CHALMERS
UNIVERSITY OF TECHNOLOGY

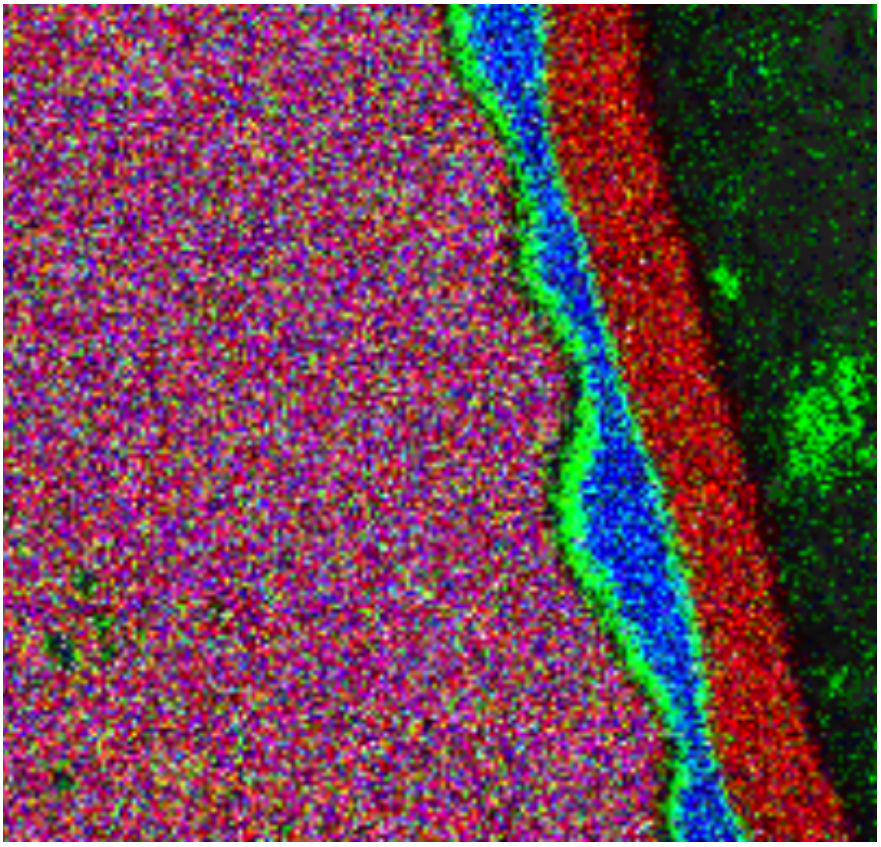

Progression of Hot Corrosion in Ni-base Superalloys for Industrial Gas Turbines

Master's thesis in Materials Engineering

CAMILO MEDINA VIRAMONTES

Department of Industrial and Materials Science
CHALMERS UNIVERSITY OF TECHNOLOGY
Gothenburg, Sweden 2019

Progression of Hot Corrosion in Ni-base Superalloys for Industrial Gas Turbines

CAMILO MEDINA VIRAMONTES

CHALMERS
UNIVERSITY OF TECHNOLOGY

Department of Industrial and Materials Science
Chalmers University of Technology
Gothenburg, Sweden 2019

Progression of Hot Corrosion in Ni-base Superalloys for Industrial Gas Turbines
CAMILO MEDINA VIRAMONTES

Supervisors: Fredrik Karlsson, Siemens Industrial Turbomachinery AB
Marie-Aude Porter, Siemens Industrial Turbomachinery AB
Examiner: Fang Liu, Department of Industrial and Materials Science, Chalmers University of Technology

Department of Industrial and Materials Science
Chalmers University of Technology
SE-412 96 Gothenburg

Cover: EDS elemental mapping overlay of Inconel 792 after 300 hour exposure to a SO_2-O_2-N_2 atmosphere at 700 °C. Showing nickel in red, aluminium in green and chromium in blue.

Gothenburg, Sweden 2019

Progression of Corrosion in Ni-base superalloys for Industrial Gas Turbines
CAMILO MEDINA VIRAMONTES
Department of Industrial and Materials Science
Chalmers University of Technology

Abstract

Siemens Industrial Turbomachinery AB is a world leading company that is dedicated to the manufacture of industrial gas turbines for energy generation. Industrial gas turbines are one of the most efficient and popular methods for providing energy to various sectors. Over the years, the use of these turbines has been extended due to the development of new materials and manufacturing methods that have improved their high temperature performance allowing them to operate at higher temperatures and leading to an increase in efficiency. Aircraft engines have benefited from these advances since they operate in a similar form as industrial gas turbines. Due to the larger market size of the aircraft engine sector in comparison to that of the gas turbine sector and the perception that both applications operate under similar conditions, the development of new materials for industrial gas turbine applications has been neglected in favour of the development of materials for the aircraft engine market. However, the current environmental issues have led to a diversification of fuels used in the gas turbines making them more susceptible to corrosion damage at their current working temperatures (1350°C) in addition to working in salt-containing environments like coasts, offshore and desserts. Therefore, it is imperative that gas turbine manufacturers develop alloys that can withstand such hazardous conditions. In this project, the progression of hot corrosion in Ni-base superalloys is evaluated in six different materials. Three of them are commercial alloys: CM247, CMSX-4 and Inconel 792; while the other three are alloys developed by Siemens, two of which are polycrystalline and the other one is a single crystal. Samples of all of the six alloys were exposed to a mixed-sulphur atmosphere at two different temperatures (700 and 850°C) for several cycles and their corrosion products were analysed using stereomicroscopy, scanning electron microscopy and energy-dispersive X-ray spectroscopy. At 700°C, the alloys underwent type II hot corrosion, and at 850°, they underwent type I hot corrosion. Based on a literature study and the results of the experiment, a reaction mechanism was proposed for each case. In terms of performance, alloys CM247 and CMSX-4 suffered the most damage, followed by a polycrystalline variation of a Siemens alloy. Inconel 792 and the single crystal variation of the Siemens alloys performed better.

Keywords: Ni-base superalloys, hot corrosion, high temperature oxidation, gas turbine.

Acknowledgements

This work was carried out in Siemens Industrial Turbomachinery AB in the department of Materials Technology and Chemistry in Finspång, Sweden. I would like to thank my two supervisors at Siemens, Fredrik Karlsson and Marie-Aude Porter for supporting me throughout the realization of this project as well as for their teachings and introducing me to the world of corrosion and superalloys. Also, my gratitude goes to the personnel of the Materials Technology department who were always welcoming and willing to help me specially to Ulrika Farnebäck, who helped me with the SEM and knows all things about all the equipment; Mikael Berggren, who helped me with the metallographic sample preparation; Artiom Alarcon, who helped me with all the small things that still matter and for always being fun and interesting to talk with; and Lennart Johansson, for always trying to integrate me more into Swedish culture.

I want to also thank my examiner Fang Liu for her words of encouragement and feedback and who always had the door open for me.

Last but not least to my family whose support and unconditional love crossed the Atlantic Ocean 24/7. Los quiero mucho y sin ustedes yo no estaría aquí. Ya sé que ni la van a leer.

Camilo Medina Viramontes, Gothenburg, June 2019

Contents

List of Figures

List of Tables

1

Introduction

1.1 Background

The high energy demand that the modern industry requires to satisfy its production needs is in constant conflict with profitability but also with the environmental repercussions that it comes with in addition to the one of the process itself. That is why a shift to more environmentally friendly and more effective methods of energy generation are being pursued by companies to ensure larger margins of revenue while keeping a discrete carbon footprint.

One of the most prominent and efficient technologies used for industrial energy generation is the gas turbine. Gas turbines consist of mainly three components: the compressor, the combustor and the turbine. The thermodynamic process starts at the compressor where air is drawn into it at a high speed and compressed which results in an increase of pressure and temperature. For a turbine to generate net power, it is necessary to add energy to the compressed air. Otherwise the blades will rotate but will not generate additional energy. This is accomplished by burning the fuel in the combustion chamber [1]. The compressed air enters then the combustion chamber where it is mixed with fuel and is burnt. Natural gas is the fuel usually used but liquid fuels and gas/liquid mixtures can be used as well. The hot gas flows into the turbine making the blades spin as the gas expands and cools down.

Gas turbines operate under a thermodynamic cycle called the Brayton cycle. The ideal Brayton cycle consists on an isentropic process[1](compression), an isobaric process (combustion), another isentropic process (expansion of the gas that moves the blades) and an isobaric process (cooling of the gas). However, real gas turbines cannot operate as the ideal Brayton cycle because the compression and the expansion cannot be truly isentropic processes. In addition, gas turbines operate as open systems so they do not reuse the same air.

In order to increase the efficiency of the gas turbines, the turbine inlet temperatures have been increased considerably in the last 40 years (modern turbines like Siemens' SGT-800 can reach net plant efficiencies of up to 58% in combined cycle power plants[3]). This has led to the development of new materials that can withstand extreme operating conditions.

[1]Isentropic process: A thermodynamic process that is both adiabatic and reversible. And there is no change of entropy [2].

With the development of new and better methodology for modelling mechanical integrity of turbine blades and guide vanes, it was realized that the new alloys developed for the aerospace industry were optimized for other regimes than the industrial gas turbines built by Siemens.

The material volume produced for the aerospace industry exceeded significantly the volume for the industrial gas turbine market which led to the situation that no significant development of new alloys for the industrial gas turbine market was done by the large casting vendors, and the right to use any new alloy could not be secured. Additionally, alloys used by Siemens were either developed in the 1960's and the 1970's when turbine inlet temperatures were relatively low or alloys that were optimized for a lifespan about 3000 hours at full load (mainly for aero applications). Hence, it led to the initiation of the project for development of two alloys.

Siemens has already used aero turbine alloys in their designs (CMSX-4 and CM247), which have sufficient oxidation resistance and excellent mechanical properties. However, these alloys have creep properties that largely exceed the design requirements. These unnecessarily good creep properties for the industrial gas turbines are achieved by sacrificing corrosion resistance. In order to obtain the creep properties necessary for the alloys used by the aerospace industry, each generation of alloys developed has gradually increased the volume fraction of the main strengthening phase used for precipitation strengthening, i.e. γ'-phase. To enable this increase and at the same time maintain stability against formation of detrimental topologically close pack (TCP) phases, the content of chromium has gradually been reduced which in turn leads to significant reduction in resistance to corrosion. As a consequence, even with the stringent requirements on inlet air filtration and fuel specifications, the use of this class of materials in industrial gas turbines imposes the risk of corrosion issues.

The older alloys used since the 1970's have a high chromium content and combination of other alloying elements that make them sufficiently resistant against corrosion. However, since they were developed at a time when the turbine inlet temperatures were in the order of 850-950°C, the resistance against oxidation is insufficient in today's design where 1130°C is considered moderate and the high end of the spectrum is up to 1350°C.

The "old" alloys involved in this study are commonly used at high temperatures but with at least one or more of the following problems: originally designed for jet engines, they have a short exposure time to high temperatures (gas turbine blades undergo longer exposure times); Their corrosion/oxidation resistance was sacrificed for the sake of strength.

The two newly developed alloys, alloy A and alloy B were designed by Siemens with the purpose of improving the material's corrosion resistance. Neither of the alloys exhibit Ti in their composition. Titanium is a relatively reactive element which enhances the mass gain of the material during the oxidation process. Removing titanium from the alloy composition should allow for a lower mass gain and a lower mass gain rate. The variation in composition should retain most of the material's

strength while increasing the corrosion resistance. In this aspect, the absence of titanium also influences the type and amount of the corrosion products formed at high temperatures.

1.2 Aim

The aim of this project is to gain a better understanding of the corrosion mechanisms of Ni-base superalloys that are used in gas turbines. This study focuses on six different materials which are CM247, CMSX-4, IN792 and three alloys developed by Siemens. The materials were studied by cyclically exposing them to a SO_2 containing atmosphere at 700°C and 850°C for up to 1500h. The oxide layers and corrosion products were analysed by different techniques such as optical microscopy, scanning electron microscopy (SEM) and X-ray energy dispersive spectroscopy (EDS).

1.3 Limitations

This work will be limited to analyse: i) the microstructure of the corrosion products along with its chemical composition, ii) the depth of corrosion penetration as a function of time and alloying elements of all samples after exposure to the corrosive environment by using optical microscopy, SEM and EDS.
Study on varying conditions like the gas flow and residence time for gas to start the corrosion attack are out of the scope of the project. In addition, the study of condensation of the alkali sulphate (if any), and where the corrosion attack initiated are not considered in this project.

2

Theoretical background

This chapter describes the theoretical foundation of the present work. In the first section, a general description of Ni-base superalloys is provided accompanied by a literature study of their microstructure, chemical composition and manufacturing methods. The second section deals with the subject of hot corrosion.

2.1 Ni-base superalloys

Ni-base superalloys are a group of alloys which can withstand loads at high temperatures without losing their mechanical properties. They are characterized for having high-strength, fracture toughness, creep resistance, corrosion and oxidation resistance and stress-rupture resistance at high temperatures [4]. This is the reason why the use of Ni-base superalloys has become more popular among the industry over the years. Sectors such as the aerospace industry, power generation and oil and gas industry rely on this type of materials to tolerate very aggressive environments, whereas conventional materials such as carbon steels, aluminium and titanium would be severely damaged.

At temperatures above 540°C, materials such as steels and titanium start to lose their mechanical properties and start to creep. Creep is the slow deformation of a material while it is subjected to a constant mechanical stress. Creep is more severe if the material is exposed to temperatures near its melting point. Very few materials have the capacity to operate at such high temperatures without suffering from creep. Ni-base superalloys' excellent creep and stress rupture resistance properties allow them to operate at temperatures above 70% of their melting point while other materials start to experience creep at 30-40% of their melting temperature. Refractory metals such as W can work well at high temperatures. However, they are not as ductile as the Ni-base superalloys.

There are two other types of superalloys: Co-base superalloys and Fe-Ni-base superalloys. Co-base superalloys can exhibit similar properties to the Ni-base superalloys but most of the time they will have a lower strength and oxidation and corrosion resistance. Fe-Ni-base superalloys (i.e. Inconel 718) are used at lower operating temperatures and are cheaper than Ni-base superalloys [5].

2.1.1 Microstructure of Ni-nase superalloys

The microstructure of Ni-base superalloys has two main components: γ and γ'. In addition, several other phases may be found in the bulk material, and whether they provide beneficial or detrimental effects to the material are governed by the desired application. The most common ones are explained below.

Gamma (γ)
γ is a non-magnetic nickel base austenitic phase. It possesses an FCC lattice structure and acts as a continuous matrix. Its ability to form a solid solution and dissolve γ' allows it to be heat treated to form fine γ' precipitates which strengthen the matrix. Further strengthening of the matrix can be achieved by adding elements such as Fe, Cr, Co, W and Mo to the solid solution [6]. The γ phase contributes to 40% (high temperature applications) up to 80% (low temperature applications) of the volume fraction of the alloy.

Gamma prime (γ')
Gamma prime possesses an $L1_2$ ordered structure. In this primitive cubic lattice, Ni atoms occupy the face-centres and Al or Ti occupy the corners. This gives the chemical formula Ni_3(Al,Ti) or Ni_3Al and Ni_3Ti alternatively [7]. γ' precipitates coherently in the γ matrix since both of them have similar lattice parameters and crystalline structure. The mismatch between the two phases is 0-1%. (figure 2.1).

Gamma double prime (γ")
This phase is composed by Ni and Nb forming a body-centred tetragonal structure (Ni_3AlNb). It is a common phase in nickel-iron-base alloys. It precipitates coherently with the matrix and induces high mismatch strains. γ" is not suitable for high temperature applications (over 650°C) because it becomes unstable and transforms into δ phase (orthorhombic Ni_3Nb) [8].

Carbides
Carbides are used as grain boundary strengtheners. In order to precipitate carbides, a concentration of maximum 0,2% carbon is required. Usual carbide forming elements are: Ta, Hf, Ti and Nb. MC type carbides can decompose into $M_{23}C_6$ and/or MC_6 carbides. $M_{23}c_6$ are formed during low temperature heat treatment. MC_6 carbides are formed when the concentration of Mo or W is more than 6 to 8 at.%.

Topologically close pack (TPC) phases
TPC phases are detrimental to the mechanical performance of the alloys. These are mainly three such phases: σ, μ and Laves phases. σ has a tetragonal structure (i.e.: FeCr, FeCrMo, CrCo). It is not common to form in Ni-base superalloys, but in iron-nickel and cobalt base superalloys. They can have an elongated or irregular globule shape. Laves phase has a hexagonal structure (i.e. Fe_2Nb, CO_2Ti, Fe_2Ti) and is most common in iron-nickel and cobalt base superalloys. It can form palettes or globule shape. μ presents a rhombohedral structure, and appears in alloys with high concentrations of Mo or W [9].

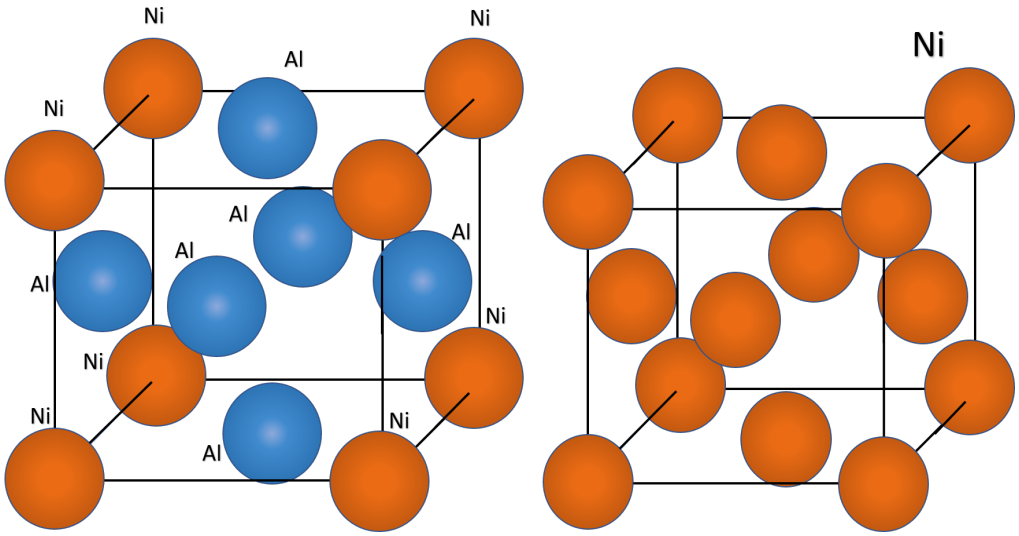

Figure 2.1: Lattice structure of gamma prime (left) and gamma (right). Notice the difference in the size of the unit cells.

2.1.2 Chemical composition

Modern Ni-base superalloys possess a very complex chemistry. Each different alloying element provides a specific property to the material. They promote the precipitation of certain species, provide corrosion and oxidation resistance, form carbides or enhance grain refinement. Table 2.1 lists the main alloying elements used in Ni-base superalloys and their effects.

Alloying elements that participate in the formation of the solid solution can increase the strength of the matrix. The strength of the material is increased because the alloying elements increase the resistance to dislocation movement. Solutes with a reasonable solubility and high hardening coefficients can result in substantial solid solution hardening and enhanced creep resistance [10]. The solubility of the alloying elements depends on a size factor which states the relationship between the atomic diameter of the element and the atomic diameter of Ni. Reference [11] provides the size factor functions for various alloying elements in Ni.

Ni-base superalloys can be divided into three major groups: cast, wrought and powder metallurgy alloys. Wrought alloys have a good fracture toughness and high strength. These properties make them suitable for applications such as milling, turning, forging and welding. Wrought alloys can be rolled or forged into sheets, turbine discs and rods. They are usually strengthened through solid solution or by the precipitation of a coherent phase (γ'). On the other hand, cast superalloys have excellent creep properties at high temperatures and can be divided into three groups: conventionally cast (CC), directionally solidified (DS) and single crystal (SC) [5, 12]. SC alloys possess better high temperature mechanical properties than their polycrystalline counterparts due to the absence of grain boundaries which can serve as stress concentration points during creep. Usually SC have a significant amount of refractory metals in their composition in order to improve their creep and

rupture resistance. However, this can lead to the formation of undesired TCP phases and they can increase the density of the material substantially. DS superalloys have columnar grains growing parallel to the growth axis. The growing direction is usually <100> [13].

Table 2.1: Effect of different alloying elements in Ni-base superalloys. Adapted from [5].

Effect	Element
Solid solution strengthener	Co, Cr, Fe, Mo, W, Ta, Re
MC carbide formers	W, Ta, Ti, Mo, Nb, Hf
M_7C_3 carbide former	Cr
$M_{23}C_3$ carbide former	Cr, Mo, W
M_6C	Mo, W, Nb
γ' former Ni_3(Al,Ti)	Al, Ti
Raises solvus temperature of γ'	Co
Hardening precipitates or intermetallics	Al, Ti, Nb
Oxidation resistance	Al, Cr, Y, La, Ce
Improve hot corrosion resistance	La, Th
Sulphidation resistance	Cr, Co, Si
Creep resistance	B, Ta
Increase rupture strength	B
Grain boundary refiners	B, C, Zr, Hf

2.2 High temperature oxidation

2.2.1 Basic thermodynamic formation of metal oxides

When metals are exposed to oxygen, they can form metal oxides:

$$\mathrm{M(s)} + \frac{1}{2}\,\mathrm{O_2(g)} \longrightarrow \mathrm{MO(s)} \tag{2.1}$$

This will create a thin oxide scale between the metal and the oxygen, separating them. Oxidation can only occur if the change of free energy (ΔG) associated with the formation of the oxide is negative.
ΔG can be described using the 2nd law of thermodynamics as:

$$\Delta G = \Delta H - T\Delta S = RTlnp_{\mathrm{O_2}}^{y/2} \tag{2.2}$$

Where ΔH and ΔS are the changes of enthalpy and entropy respectively. T is the absolute temperature, $p_{\mathrm{O_2}}$ is the oxygen partial pressure and y/2 is the number before $\mathrm{O_2}$ in the balanced reaction equation of the respective oxide. In order to form an oxide, the partial of pressure of the oxygen in the atmosphere has to be higher than the partial pressure of oxygen in the oxide:

$$p_{\mathrm{O_2}} = \exp\frac{2\Delta G}{yRT} \tag{2.3}$$

Ellingham diagrams plot the standard free energy of oxide formation as a function of temperature. They allow for the comparison of the relative stabilities of compounds such as oxides, sulphides and carbides. The lower a point is in the diagram, the more stable that species is.

The Ellingham diagrams can be used for three applications: 1) to determine the oxygen partial pressure for oxide formation at any temperature; 2) to obtain the relative stability of the metal oxide and to see if it will form under certain oxidizing condition; 3) to evaluate the metals to see if they can be used to reduce a metal oxide [14, 15].

Since the surface atoms of a material have fewer neighbours than the ones in the bulk material, they are more reactive and seek to saturate their missing bonds. In an oxidizing atmosphere, oxygen molecules will be adsorbed by the surface and dissociated to be later dissolved into the metal [17]. As mentioned earlier, a thin oxide scale is formed between the oxygen and the metal. For further reaction, it is necessary for at least one of the reactants to diffuse through the oxide by $solid-state\ diffusion$. Either the oxygen can penetrate and diffuse to the metal-scale interface or the metal can be transported through the scale to the scale-gas interface.

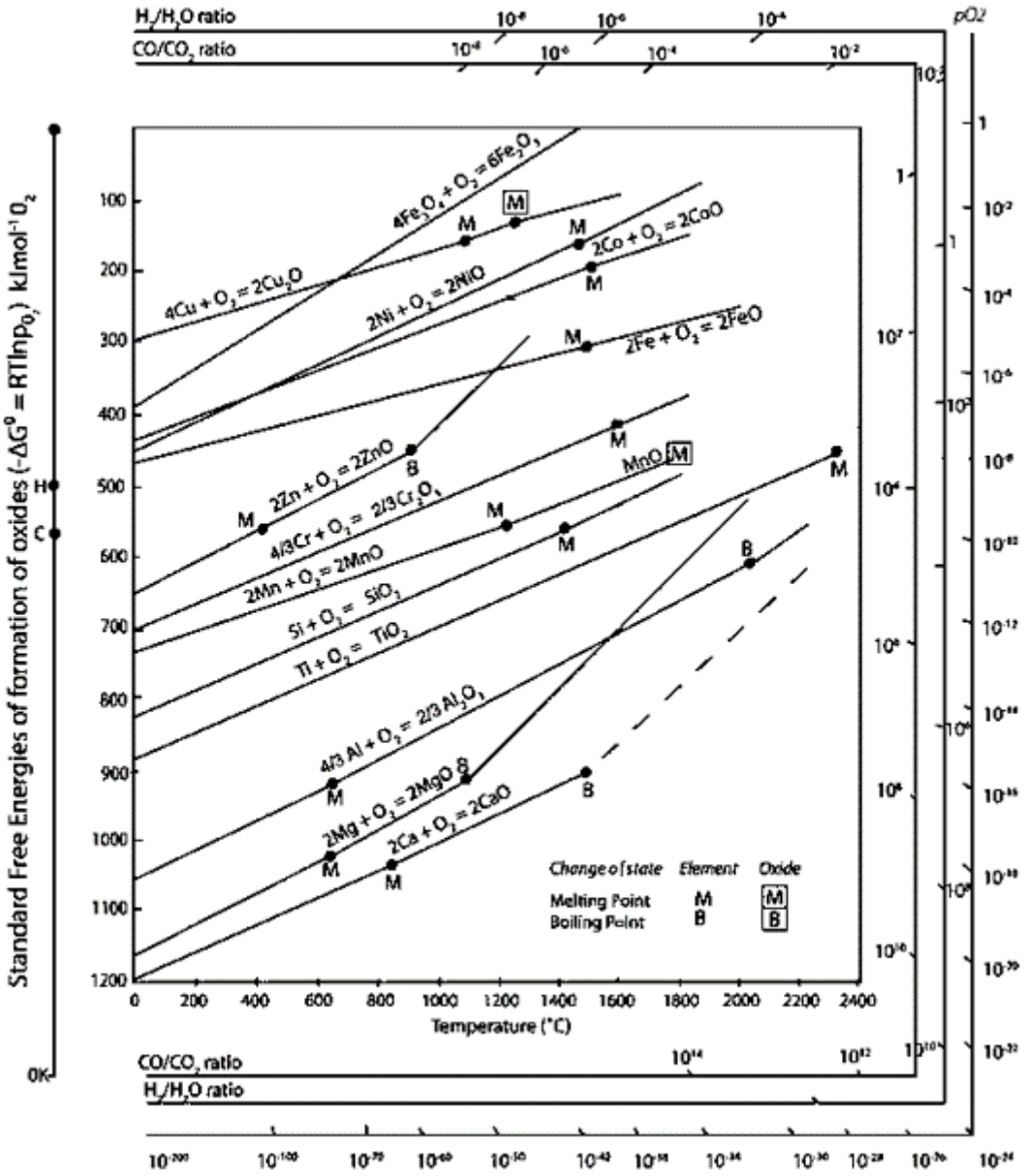

Figure 2.2: Ellingham diagram for various oxides [16].

2.2.2 Transport mechanisms

The transport of ionic species through the oxide lattice depends on the number of defects on its lattice. There are three types of defects: point defects, linear defects and plane defects.

Point defects
Point defects consist of either vacancies (sites where a constituent atom is missing) or interstitial atoms. Since metal oxides are ionic compounds, they can present two of the following ionic defect structures: highly stoichiometric ionic structures and non-stoichiometric structures.

Highly stoichiometric ionic structures: These compounds present two types of defects which are *Schottky defects* and *Frenkel defects*. In Schottky defects, both cations and anions are mobile. The ionic mobility is related to the presence of ionic vacancies. An equivalent number of cations and anions are missing in order to maintain electroneutrality. In Frenkel defects, only cations are mobile. It is assumed that the anion sub-lattice is perfect, but the cation sub-lattice has vacancies. Interstitial cations maintain the electroneutrality [18].

Non-stoichiometric ionic structures: These are the most common structures for metal oxides. They are classified as semiconductors and can be either *n-type* or *p-type* semiconductors. N-type behaviour can arise from metal excess (abundance of interstitial metal ions) and oxygen deficit (oxygen vacancies in the lattice). On the other hand, p-type behaviour occurs when there is a metal deficit and oxygen excess [17].

Linear and planar defects
Line defects are also called *dislocations*. There are basically two types of dislocations: *edge* and *screw*. Planar defects include external surfaces, grain boundaries, twins, low-angle boundaries, twists and stacking faults [19]. Linear and planar defects are high diffusivity paths due to the low activation energy they require for diffusion in comparison to the lattice diffusion. They require around 50 - 70% of the activation energy of lattice diffusion and their diffusion coefficients are 10^4 - 10^5 times larger [17, 20]. This type of diffusion is also called *short-circuit diffusion*. At low temperatures, this type of diffusion predominates and at high temperatures, both lattice and short-circuit diffusion can happen [17].

2.2.3 Rate of oxidation

Metal oxide growth can be ruled by either one of the following two laws: the *linear rate law* and the *parabolic rate law*.

Linear rate law
As the name implies, the growth of the oxide scale proceeds at a constant rate as described by equation 2.4.

$$x = k_l t \tag{2.4}$$

Where x is the scale thickness, k_l is the linear rate constant and t is the time [21]. This behaviour is observed when the rate-limiting step is a phase-boundary process. Since the scale is thin at the beginning of the process, diffusion through it is not likely to be rate limiting. In addition to the initial oxide formation, this is also observed in case of spallation and re-oxidation of the metal [21, 22].

Parabolic rate law
When the diffusion of cations and/or anions is the rate-determining process, then the metal oxide growth is governed by the parabolic growth. It is considered that the diffusion rate is constant through the scale. As the thickness of the scale increases, the reaction rate decreases:

$$x^2 = k_p t \tag{2.5}$$

Two conditions must be fulfilled in order for parabolic growth to occur [17]:
1. The oxide layer is compact and adherent.
2. As mentioned above, the migration of ions through the oxide layer is rate-determining.

2.2.4 Oxidation of Ni-base alloys

Ni-base alloys used at high temperatures require the formation of a stable protective oxide layer. For the oxide to be considered protective, it needs to satisfy certain conditions [23]:

1. It should not have a high vapour pressure.
2. It should not be a liquid.
3. It should not form a powder.
4. It should maintain its integrity during heating and cooling, so it should not undergo a phase transformation in temperature range of interest.
5. It should not react with water vapor at low temperature.

The alloying elements that are most commonly used to form a protective oxide scales in Ni-base alloys are Cr, Al and Si. When an alloy has several alloying elements, the composition of the oxide passive layer depends on which oxide is more thermodynamically stable at the given conditions.

Chromia-forming nickel alloys
In Ni-Cr binary alloys, there have been identified three compositional regimes that exhibit different oxidation behaviours [24, 25, 26]:

1. *Low Cr* (Cr > 10wt.%): The alloy forms an external NiO layer and a duplex internal scale made of porous NiO - $NiCr_2O_4$ islands and NiO - Cr_2O_3 islands.

2. *Intermediate Cr* (18wt.% > Cr > 10wt.%): The oxide growth goes through a process called *transient oxidation*. This results in the formation of outer scales growing on top of each other. The scale in the metal-scale interface is composed by Cr_2O_3 and the scale on the scale-gas interfaces is made of NiO.

3. *High Cr* (20wt.% ≥ Cr ≥ 18wt.%): An external continuous Cr_2O_3 scale is formed. Concentrations above 20% are not usually used in order not to limit the addition of other alloying elements.

Alumina-forming nickel alloys
Similar to the chromia forming alloys, there are three regions of oxidation which yield different products according to the concentration of Al in the material [22, 27]:

1. *Low Al* (Al < 6 wt.%): A NiO external oxide scale is formed along with and internal Al_2O_3 + $NiAl_2O_4$.

2. *Intermediate Al* (17 wt.% > Al > 6 wt.%): Initially, Al_2O_3 is formed but it cannot be sustained so it is replaced by a NiO + $NiAl_2O_4$ + Al_2O_4 mixture.

3. *High Al* (Al > 17 wt%): External Al_2O_3 is formed.

The addition of Cr to Al forming alloys promotes the selective oxidation of Al. Within a range of 18-20 at.% Cr the amount of Al required for selective oxidation is reduced from 22 at.% to 10 at.% [28] . A Cr content of 10 wt.% will enhance the selective oxidation of Al in the alloys with less than 5 wt.% [29].

2.2.5 Reactions with sulphur and mixed environments (Metal-sulphur-oxygen)

Thermodynamically stable sulphides can only form when the potential of sulphur is high enough. In practice, the reactive gas does not contain pure sulphur but sulphur-containing compounds which are usually sulphur oxides, e.g. SO_2 and SO_3. In the case of SO_2, the equilibrium reaction is given by:

$$SO_2 \rightleftarrows O_2 + \frac{1}{2} S_2 \tag{2.6}$$

The sulphur partial pressure becomes:

$$p_{S_2} = K \frac{(p_{SO_2})^2}{(p_{O_2})^2} \tag{2.7}$$

The formation of sulphides results from a high partial pressure of SO_2 and a low partial pressure of O_2 while sulphates are formed with a high partial pressure of both SO_2 and O_2 [30]. The formation of oxides is therefore a product of a high partial pressure of O_2 and low partial pressure of SO_2.

$$p_{O_2} > \frac{a^2_{A_nO}}{a^{2n}_A} \exp \frac{2\Delta G^o_1}{RT} \tag{2.8}$$

$$p_{S_2} > \frac{a^2_{A_mS}}{a^{2m}_A} \exp \frac{2\Delta G^o_2}{RT} \tag{2.9}$$

Where n is the number of neutral atoms of metal A reacting with $\frac{1}{2}O_2$ to form an oxide with the form A_nO and ΔG^o_1 is the change of free energy of:

$$nA(s) + \frac{1}{2}O_2(g) = A_nO(s) \tag{2.10}$$

And m is the number of neutral atoms of metal A reacting with $\frac{1}{2}S_2$ to form a sulphide with the form A_mS and ΔG^o_2 is the change of free energy of:

$$mA(s) + \frac{1}{2}S_2(g) = A_mS(s\,or\,l) \tag{2.11}$$

For SO_3 the equilibrium reaction is:

$$SO_2 + \frac{1}{2}\,O_2 \rightleftharpoons SO_3 \tag{2.12}$$

At high temperatures, the partial pressure of SO_2 is higher than for SO_3 so the equilibrium favours the left side of the equation. The partial pressure of SO_3 is favoured at lower temperature.

The sulphidation rate is highly related to the temperature. The sulphidation of pure nickel produces NiO, NiS and $NiSO_4$ at a high corrosion rate [31]. Higher temperatures than the one at which the corrosion rate is maximum reduce the corrosion rate. The temperature at which the corrosion rate peaks is dependent on the composition of oxidizing gas.

2.3 Hot corrosion

Hot corrosion can be defined as the accelerated oxidation attack caused by a salt deposit, commonly a sulphate. Salt deposits can be originated in environments where the alloys are exposed to, mainly, combustion, e.g. gas turbines. During combustion, the sulphur from the fuel forms sodium sulphate (Na_2SO_4) after reacting with sodium chloride (NaCl). The newly formed salt is deposited on the hot-section components [32]. The factors that can influence the severity of the attack are the amount of the deposit and its composition, gas composition, temperature, temperature cycling, erosion, the alloy's composition and microstructure [33]. The resistance of an alloy to hot corrosion attack highly depends on whether the salt deposit melts or not.

The process of hot corrosion is divided into two periods: the *incubation period* and the *propagation period*. During the incubation phase, the metal-deposit interface is altered in a way that facilitates the attack. This process is realized by depleting the metal of the alloying element which creates the passive oxide layer, incorporating an element from the deposit into the alloy, dissolving oxides into the salt or the occurrence of cracks in the scale [34]. The propagation period can occur by two different modes: *basic fluxing* and *acidic fluxing*. The basic fluxing mechanism consists of the reaction of the passive oxide scale with the oxide ions of the melt to create soluble species. In acidic fluxing, the ions of the oxide layer dissolve into the melt.

2.3.1 High temperature hot corrosion (HTHC)

HTHC is also known as hot corrosion type I. It occurs in the temperature range of 800-950°C. The corrosion products form a layered porous scale on the surface of the alloy and internal sulphidation of the alloy and alloying elements is observed. The kinetics of the propagation stage follow the acidic dissolution of the oxide scale. The acidic components are namely SO_3 and refractory metal oxides such as MoO_3 and WO_3.

2.3.2 Low temperature hot corrosion (LTHC)

LTHC is also referred to as hot corrosion type II. LTCH develops in the temperature range of 600-800°C. This type of hot corrosion is influenced by SO_3 since the partial pressure of SO_3 is higher than the one of SO_2 in this temperature range. Alloys affected by this type of corrosion exhibit pitting morphology. There is little to no internal sulphidation of the alloy [35].

Similarly to the oxidation rate, the corrosion rate is governed by temperature and can reach a maximum value at certain temperatures (figure 2.3).

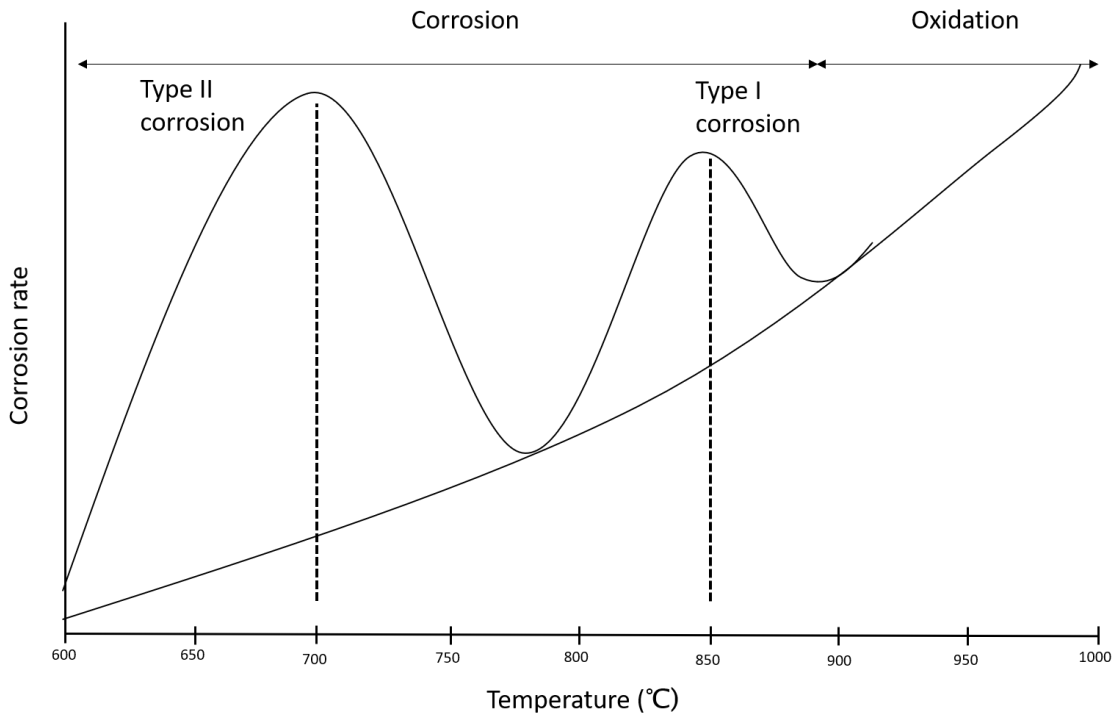

Figure 2.3: Corrosion rate for type I and type II hot corrosion. Adapted from [22].

3
Methodology

This chapter describes the materials used in this study of which three of them are known commercial alloys used for industrial gas turbine applications (CMSX-4, CM247 and Inconel 792) and the other two are new alloys developed by Siemens, which will be referred to as alloy A and alloy B. The second part of this chapter deals with the sample preparation and testing conditions used. The final section provides a brief description of the analysis techniques used to characterize the corroded samples.

3.1 Investigated materials

3.1.1 CM247 and CMSX-4

Alloy CM247 is a directionally solidified (DS) cast Ni-base superalloy with low concentration of carbon. The microstructure consists of a γ matrix with a 62% volume of γ' as intermetallic phase. Originally, the alloy was not developed for DS casting, but for equiaxed parts. In order to improve its DS-casting properties grain boundary cracking during casting had to be mitigated. The grain boundary cracking resistance is obtained by the addition of Hf in the range from 1.4% to 2%. This leads to the formation of HfC-type carbides on the grain boundaries. Its high resistance to grain boundary cracking during casting, in addition to its high creep strength and excellent oxidation resistance make it suitable for applications in turbine blades and vanes [36, 37].

CMSX-4 is a 2nd generation single crystal alloy with no carbon content. This type of alloys benefit from the strengthening effects of Re (3% wt.). Re strengthens the material by partitioning to the γ phase causing a delay in the coarsening of γ' and increasing the γ/γ' misfit. Small Re clusters interfere with the dislocation movement therefore increasing the strength of the material. Re that partitions to the γ' phase also strengthens the γ' phase. CMSX-4 has exceptional mechanical fatigue properties due to the absence of residual γ/γ' eutectic phase, carbides, inclusions (oxides, sulphides and nitrides) and micro-porosities. [38].

Both of these alloys are Al_2O_3 formers.

3.1.2 Inconel 792 (IN792)

IN792 is a conventionally cast Ni-base superalloy. It is widely used in aircrafts and industrial gas turbines because of its high temperature mechanical properties and hot corrosion resistance. Its microstructure is composed mostly by a 1:1 γ/γ' ratio (with cuboidal γ' precipitates) and $M_{23}C_6$ carbides. Small amounts of borides, eutectics and topologically close-packed (TCP) phases can also be present [39]. Its high Cr and low Al content allows IN792 to form a protective Cr_2O_3 layer at high temperatures protecting the alloy from corrosion.

3.1.3 Alloy 'A' and Alloy 'B'

Alloy A is a conventional cast Ni-base superalloy developed by Siemens with the purpose of substituting IN792. This study utilized two variations of this alloy which will be called "A-1" and "A-2".

A-1 is intended to be used in first stage blades and vanes. Therefore, high oxidation resistance is needed. In order to maximize this property, Ti is not used as an alloying element since it is known to be a very reactive element in oxidizing atmospheres. Corrosion resistance is achieved by adding Cr and removing elements such as Mo. Although creep resistance is relevant, it does not need to be at very high levels. Variation A-2 sacrifices oxidation resistance in favour of better mechanical properties. Its intended application is in last stage components. Titanium is present at some extent.

Alloy B is a single crystal Ni-base alloys developed also by Siemens. It follows the same design approach as A-1 in terms of increasing oxidation and corrosion resistance. Ti is not present in this alloy.

Table 3.1: Nominal composition of investigated materials in wt.% with Ni as balance.

	Cr	Co	Re	Mo	W	Al	Ti	Ta	Hf	Zr	C	B	Ce	Si
CM247	8	9,5	0	0,5	9,5	5,65	0,7	3,2	1,4	0,01	0,07	0,015	0	0
CMSX-4	6,5	9,5	3	0,5	6,5	5,6	1	6,5	0,1	0	0	0	0	0
IN792	12,5	8,5	0	1,8	4,2	3,5	4,2	4,2	0,5	0,01	0,07	0,015	0	0
Alloy A-1	12,5	5	0	1-3	2-4	5-6	0	7-8	0-2	0-2	0-2	0-2	0-2	0-2
Alloy B	15	5	0	1-2	3-5	4-5	0	6-9	0-2	0	0-2	0	0-2	0-2

3.2 Sample preparation for high temperature and gas exposure

3.2.1 Initial conditions

All test cylinders were machined by the Department of Metallurgy and Materials at the University of Birmingham. Samples from Alloys A and B were manufactured by the same department. All samples underwent surface grinding to eliminate the oxide layer caused by the HIPping. The samples were 10mm in diameter and 10 mm in height.

3.2.2 Salt spraying

The salt spraying procedure was performed at RISE Kista in Stockholm.

Samples were placed in a holder as shown in Figure 3.1. Then the holder with the samples was placed on top of a pre-heated stove at 100°C in order to be able to evaporate the solvent from the spraying solution when it came in contact with the sample. The samples were sprayed horizontally with a salt mixture of Na_2SO_4 and K_2SO_4 with a molar ratio of 80/20 and a concentration of 0,125 M. The spraying was performed manually by an operator. The samples were sprayed four times before being rotated to a new position where they were sprayed again (figure 3.2). This was done in order to ensure a uniform salt deposition which corresponded to a 0,5μg/cm^2/cycle deposit which is equal to a salt flux of 5μg/cm^2/h. The spraying was performed before each thermal cycle.

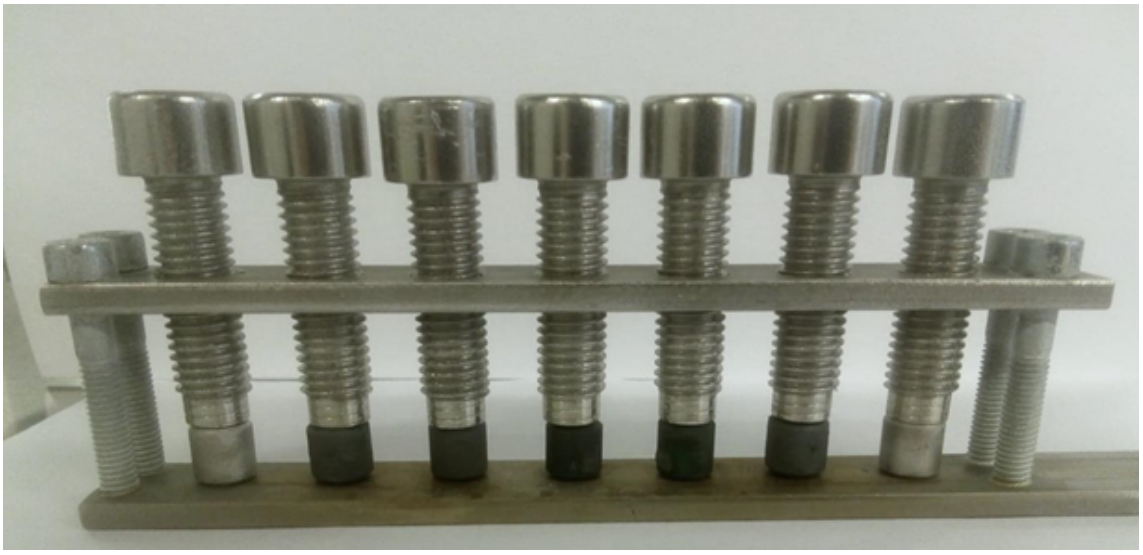

Figure 3.1: Sample holder with mounted samples. The samples at both far ends are dummy samples.

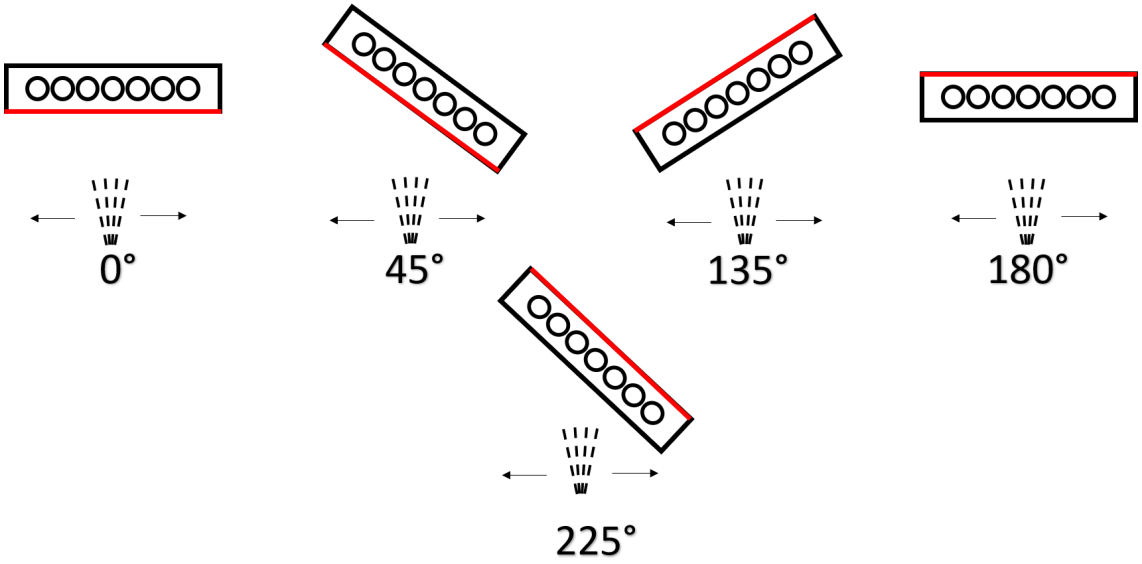

Figure 3.2: Spraying method. Figure depicts a schematic top view of the sample holder with the samples. The samples were sprayed in the direction of the arrows before being rotated to the next angle. A red line is used as a reference point.

3.3 High temperature and SO_2 exposure

The samples were placed in a cordierite crucible. The crucible was introduced 64 cm into an Elite® three-zone horizontal furnace (model TMH12/75/750). Alumina fibres were placed at both ends of the furnace to serve as a thermal insulator. The furnace was then sealed and purged with Ar for 15 minutes. A mixture gas of 300 vol. ppm SO_2 -14,6% O_2 -N_2 balance was introduced until the internal pressure was 1 bar. Heating was then started. Two test temperatures were used: 700 and 850°C. The samples were subjected to thermal cycles with 100 hours per cycle. Gas mixture was kept flowing for the entire duration of the cycle. For the 700°C test run, the samples were taken out of the furnace for analysis at 100, 300, 500 h. For the 850°C test run, the samples were taken out of the furnace for analysis at 100, 300, 500, 1000 h. Alloy A and alloy B samples were only tested until 500 hours at 850°C.

3.4 Metallographic preparation

All samples were mounted in a bakelite/carbon resin in order to perform a cross-section analysis using optical microscopy and SEM/EDS. The grinding and polishing steps are described in tables 3.2 and 3.3 respectively.

Table 3.2: Grinding conditions

Grinding paper	Grit	Cooling agent	Force (N)	Time (min)
SiC	120	Water	30	1
SiC	220	Water	20	1
SiC	320	Water	15	1
SiC	500	Water	20	1

Table 3.3: Polishing conditions

Polishing disc/cloth	Suspension	Force (N)	Time (min)
MD-Largo	DiaPro Allegro/largo 9 μm	15	4
MD-DAC	DiaPro Dac 3 μm	30	3
MD-Nap	DiaPro Nap-B 1 μm	25	4
MD-Chem	OP-S 0,04 μm	25	4

3.5 Characterization methods

3.5.1 Optical microscopy (OM)

A stereo microscope was used to make an assessment of the samples after being exposed to the corrosive atmosphere and high temperature. Optical microscopes use primarily two sets of lenses to provide the magnification of an object: Objective lens and the eyepiece. The objective lenses collects light from the object, creating an inverted and magnified real image, while the eyepiece further magnifies the image and inverts the real image obtained by the objective lens. Unlike usual light microscopes, stereo microscopes use reflected light instead of transmitted light. Stereo microscopes work at lower magnifications but have a longer working distance and depth of field which is useful to observe irregular surfaces. Before mounting the samples into bakelite, the external surface of the samples was examined. Stereo microscopy allows a detailed view of the external oxide scales and morphology. The samples were examined again after being mounted in bakelite to analyse the loss of cross-sectional area as a function of time. Stereo microscopy also served to identify regions of interest for subsequent analysis.

3.5.2 Scanning electron microscopy (SEM) & Energy Dispersive X-ray Spectrometry (EDS)

The corroded specimens were analysed using a Jeol JSM 6000 scanning electron microscope equipped with an energy dispersive X-ray detector. The SEM uses an electron gun to generate an electron beam that can have an energy value anywhere in the range of 100-30,000 electron volts (eV). The beam is focused by an array of electromagnetic lenses. This way the spot size can be reduced, increasing the resolution, while not losing so much of the electrons from the original beam. When the electron beam interacts with the sample, it generates different signals that are picked up by the detectors which are then used to generate the image. SEM detectors deal with two different types of signals: backscattered electrons (BSE) and secondary electrons (SE). SE are generated when the electrons are in-elastically scattered when they interact with the sample meaning that they lose energy. SE are used to generate topographical images. BSE, on the other hand, occur when the electrons from the electron beam are elastically scattered (they are deflected with a minimal loss of energy). BSE provide compositional contrast. Higher atomic number (Z) elements deflect more electrons, thus they will appear lighter in the image, while low Z elements deflect less electrons making them appear darker.

SEM was used to analyse the cross-section of the corroded specimens. The secondary electron mode was used to obtain topographical images of the corrosion layers. The acceleration voltage was set at 20 keV. Backscattered electron mode was used to acquire a compositional contrast among the different corrosion products on the cross-section.

Characteristic X-rays are also generated by the interaction between the electron beam and the sample. However, a special detector is needed to identify them. X-rays are generated when an outer shell electron has to fill a vacant position in an inner shell of an atom leading to the release of the additional energy corresponding to the energy difference between the two shells. This vacancy is created when a high energy electron (or any other high-energy particle) collides with an inner shell electron causing it to be ejected from the atom. When the X-rays interact with the Li drifted Si detector, they will generate electron-hole pairs that are measured. EDS analysis can also yield quantitative results. However, light elements such as O, N, C, and B are hard to detect due to their low efficiency in generating X-rays.

EDS elemental mapping and point analysis were performed on the surface of the samples before mounting them in bakelite to identify the chemical composition of the outermost oxide layers. For the cross-section, elemental mapping, line scan and point analysis were used to identify the chemical composition of the different oxide layers as well as internal corrosion products that formed in the material.

4

Results

This chapter shows the results obtained on this project.

4.1 Corrosion test at 700°C

4.1.1 CM247 and CMSX-4

After the initial 100h exposure, no significant internal or external corrosion nor oxidation products could be identified by the cross-sectional analysis using SEM. CMSX-4 appears to have a thin layer of internal sulphidation but it was too small to be analysed and identified.

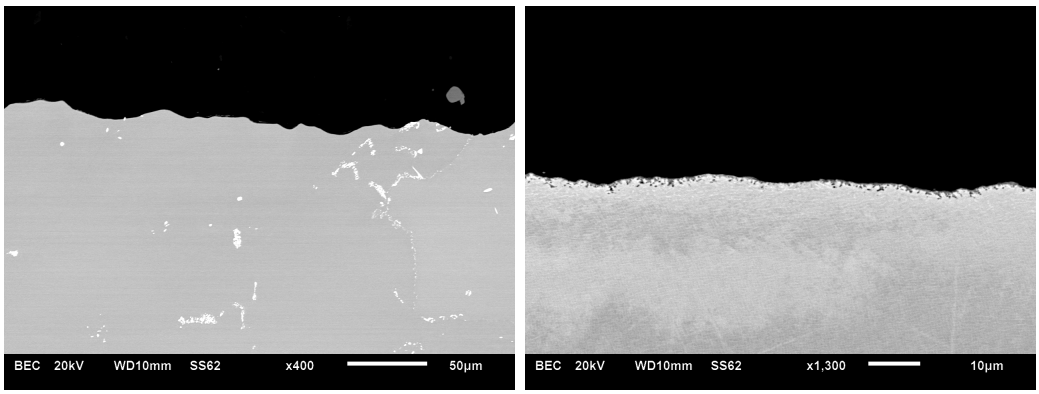

(a) **(b)**

Figure 4.1: Comparison between (a) CM247 and (b) CMSX-4 at 700°C/100h

After 300h, both materials exhibit type II hot corrosion morphology. The oxide scale buckled and deformed the material below it. This may be due to the compressive stresses the scale is subjected to while growing. The oxide scale formed on CMSX-4 has a more compact appearance than the one formed in CM247 which exhibits some voids near the interfaces between different oxide layers. Longer exposure times did not show any major changes in the composition or morphology of the layers. They just increase their size. The thickness of the corrosion products on alloy CM247 is around 110 μm and 70 μm in CMSX-4 after 500 h.

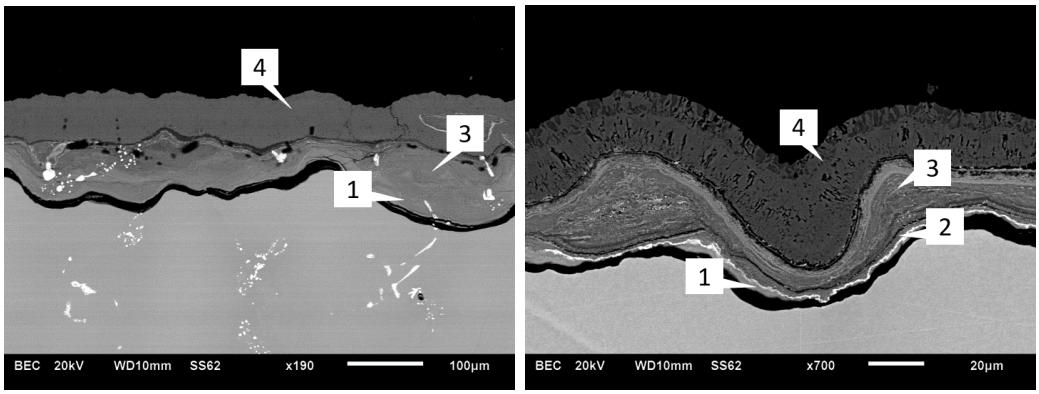

(a) **(b)**

Figure 4.2: Comparison between the oxide scales formed on (a) CM247 and (b) CMSX-4 at 700°C/500h.Different layers of corrosion products are identified **1:** S-enrichment **2:** Ni-oxide, **3:** Cr-, Al-oxides, **4:** Ni-oxide.

4.1.2 IN792

IN792 shows the usual morphology of type II corrosion. Line scan analysis in the pits around the surface of the material reveals the distribution of Cr, Al, S, Ni, O and Ti (figure 4.3). Corrosion products consist of a sulphur enriched bottom layer, followed by different Cr- and Al-oxides. The external oxide scale is composed of porous Ni-oxide. The thickness of the corrosion products was 40μm within the first 100h. After 500h, the thickness of the corrosion products is larger than 90μm.

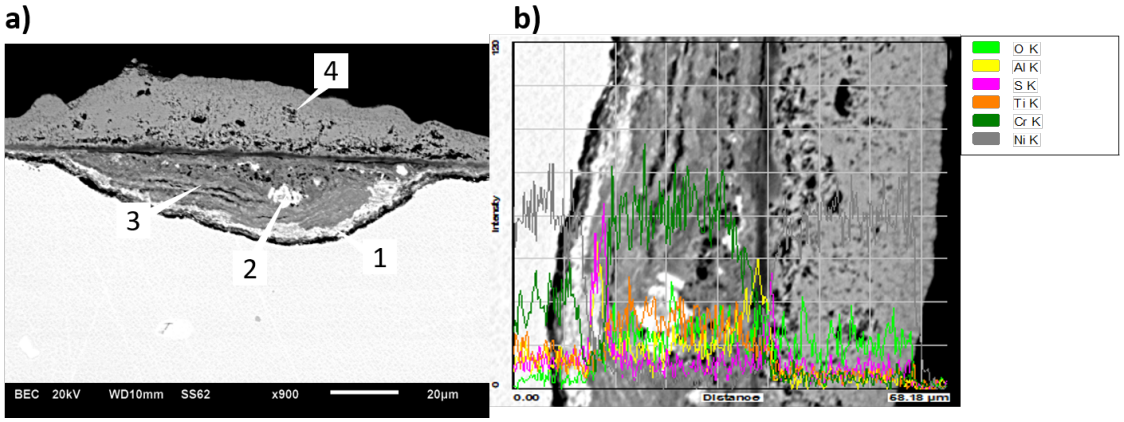

Figure 4.3: IN792, 700°C/100h. a) SEM cross-section. **1:** Sulphur enrichment, **2:** Ta_2O_5, **3:** Cr-, Al- oxides, **4:** NiO. b) Line scan analysis of the corrosion products of a).

Figure 4.4 shows the EDS elemental mapping of IN792 after being exposed for 500 h. A double layer of Ni-oxides can be observed; one in between Al and Cr oxides and the other one at the top surface. The scale shows good cohesion within itself but not to the alloy.

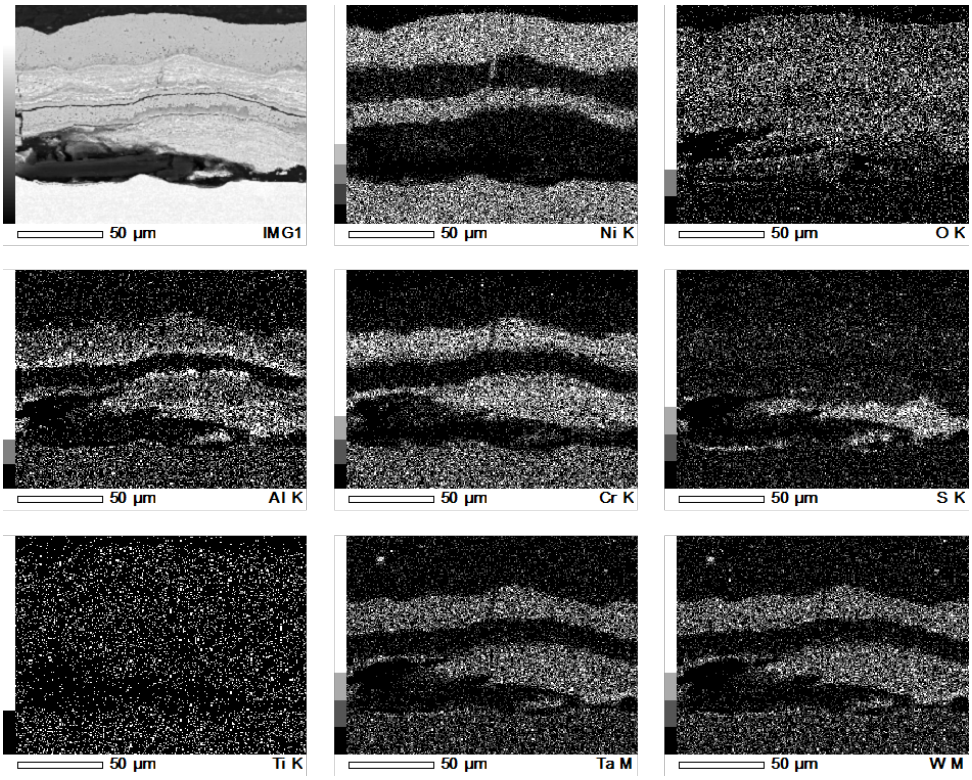

Figure 4.4: EDS elemental mapping of IN792, 700°C/500 h.

4.1.3 Alloys A-1 and A-2

After 100h, alloy A-1 presents type II corrosion morphology. The depth of the attack is in the range of 3 - 5μm. Carbides near the surface generate additional stress to the growth of the passive oxide layer (figure 4.5a). A sulphur enriched zone is located at the metal-oxide interface. It contains traces of other elements such as Ni, Cr, Al and Ta. It is followed by a Ni-, Al- oxide layer. On the surface porous NiO was observed. After 300h, the scale grows to a thickness of 40 μm and some sections have detached from the alloy. Carbides can be observed embedded into the oxide scale. At 500h, the thickness of the corrosion layer became larger than 120 μm. Similar to IN792, the formation of a double NiO layer was also observed.

Alloy A-2 shows less internal oxidation after 100 h in comparison with A-1. The depth of penetration is up to 3 μm. The oxide layer is thin and compact, composed of Ni-, Cr- and Al-oxides. Carbides can be found near the surface under the thin oxide layer. A small sulphur enriched layer is observed with small black inclusions which could not be analysed due to their small size. The depth of attack extends up to 50 μm after 300 h. Carbides are embedded in the scale in a similar manner as in A-1. After 500h, the depth of attack did not increase significantly (69 μm). The nature of the corrosion products remains similar to the one observed in the 300h sample.

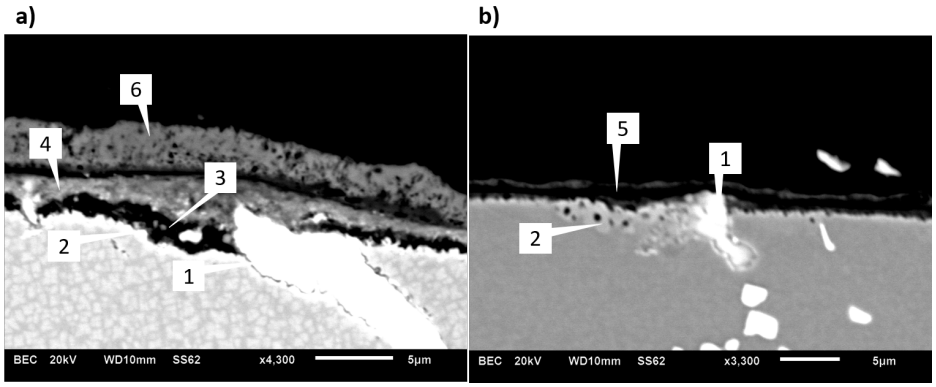

Figure 4.5: a) Alloy A-1, 700°/100h. Type II corrosion morphology after 100 h. b) Alloy A-2, 700°/100h. **1:** Carbide, **2:** S-enriched layer, **3:** Cr, Al- oxides, **4:**Cr-, Al-oxides, **5:** Ni-, Cr-, Al- oxides, **6:** NiO.

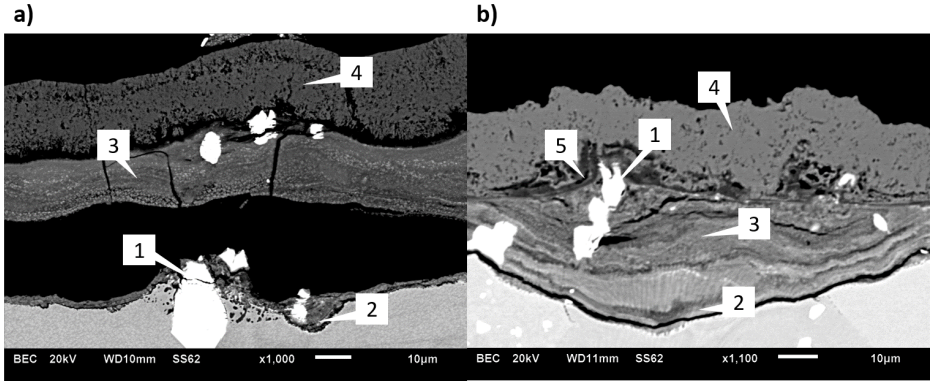

Figure 4.6: a) Alloy A-1, 700°/300h. Carbide fracturing the oxide scale. b) Alloy A-2, 700°/300h. Carbides embedded in the corrosion products. **1:** Carbide, **2:** S-enriched layer, **3:** Cr-, Al- oxides, **4:** NiO, **5:** Ti- oxides.

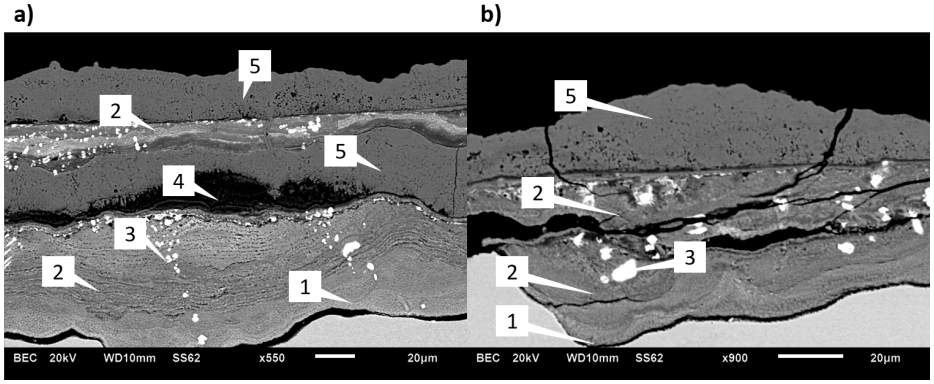

Figure 4.7: a) Alloy A-1, 700°/500h. b) Alloy A-2, 700°/500h. **1:** S-enriched zone, **2:** Cr-, Al- oxides, **3:** Trapped carbide, **4:** Al-oxide, **5:** NiO.

4.1.4 Alloy B

No corrosion or oxidation products were found in the cross-section analysis of the samples. All three samples present a rough surface which means that the pits were created but the product spalled off.

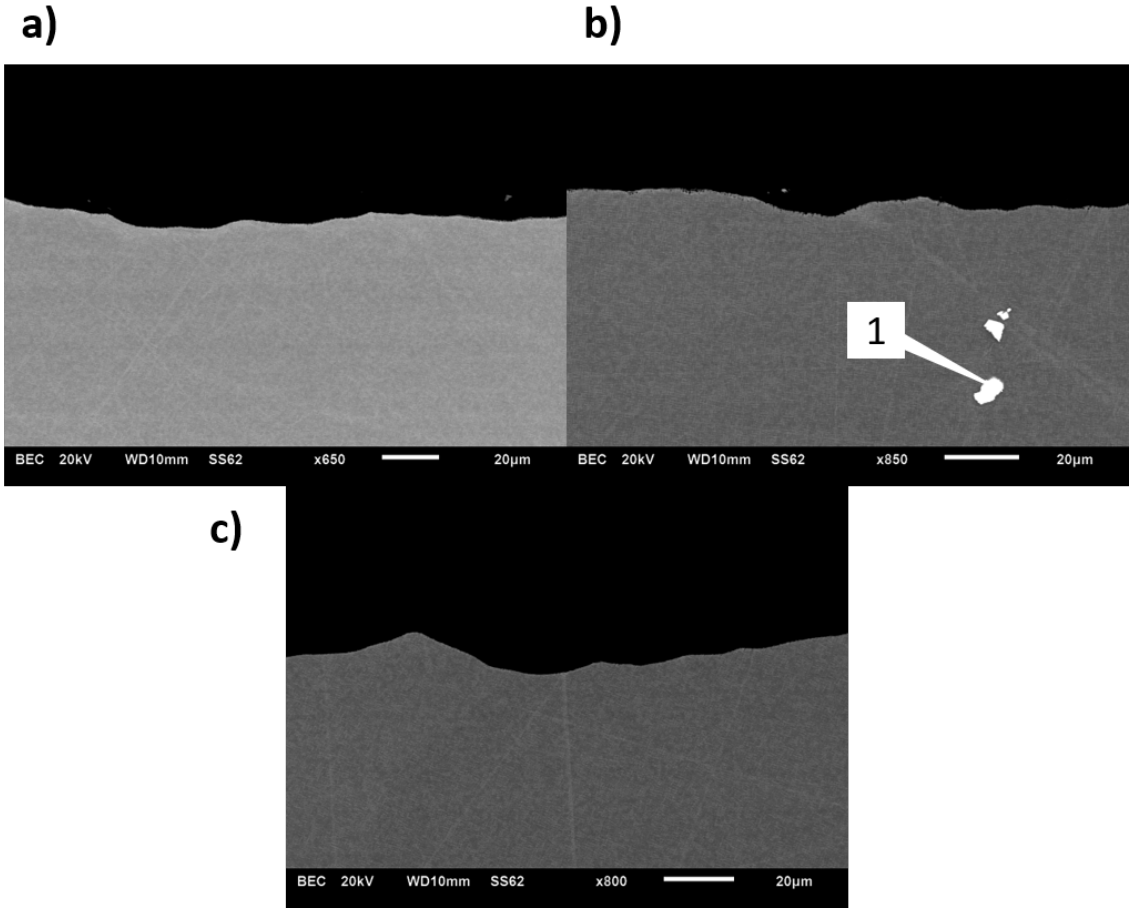

Figure 4.8: a) Alloy B, 700°C/100h. b) Alloy B, 700°C/300h. c) Alloy B, 700°C/500h. **1:** Carbides.

4.2 Corrosion test at 850°C

4.2.1 CM247 & CMSX-4

Both alloys exhibit type-I corrosion morphology. A porous non-protective oxide layer has formed uniformly around the samples. This oxide layer shows several cracks in longitudinal direction. CMSX-4 shows a better resistance to hot corrosion after the first cycle than CM247. The oxide scale in CMSX-4 at this point formed a layered structure. However, after 3 cycles the damage has extended to a similar level across both samples. After 500h, the samples start to show severe spallation of the oxide scales. The retardation of the propagation of the corrosion process in CMSX-4 is most likely due to its lack of grain boundaries, which are known to be a vulnerable pathway for corrosion. In addition, the absence of carbides in CMSX-4 might be vital since they hinder the formation of a protective oxide scale.

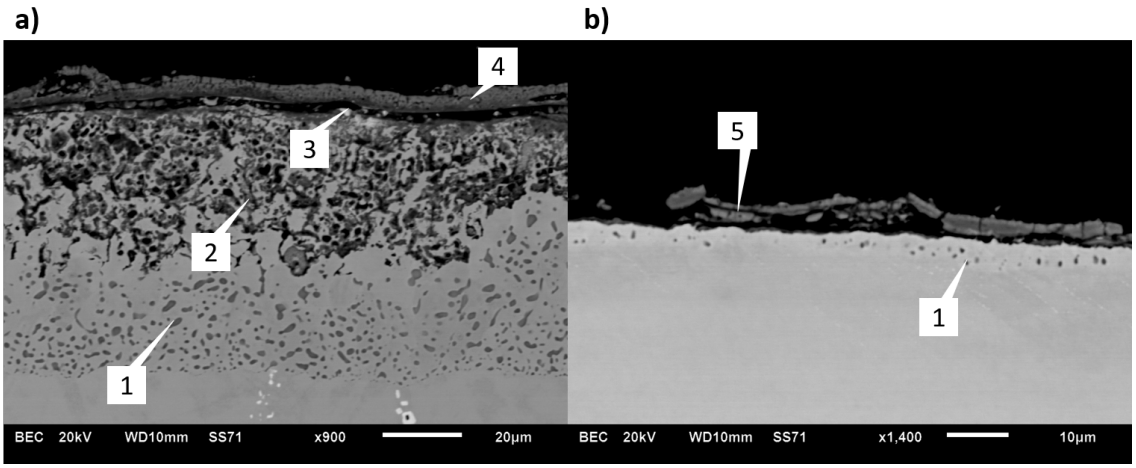

Figure 4.9: a) CM247 850°C/100h. b) CMSX-4 850°C/100h. **1:** Cr-sulfides, **2:** Cr-, Al-oxides, **3:** Ni-W-oxides, **4:** NiO, **5:** Ni-, Cr-, Al-oxide.

The internal corrosion products consist of a sulphidation front that is composed mostly of Cr-sulphides and an inner oxidation layer formed by porous Cr-oxides and Al-oxides. Beneath the external NiO layer small particless made of W-oxides or a Ni-W-oxide are found.

The internal sulphidation and corrosion products precipitate in a Ni-rich matrix (74,91 at.%) caused by the depletion of nearby alloying elements. TaS_2 was found as elongated needle-shaped precipitates next to the CrS precipitates (figure 4.10). The thickness of the corrosion products can reach up to 500, 730 and 1160 μm for CM247 after 300, 500 and 1000 h, respectively. For CMSX-4, the thickness of the corrosion products can reach 313, 887 and 969 μm after 300, 500 and 1000 h, respectively.

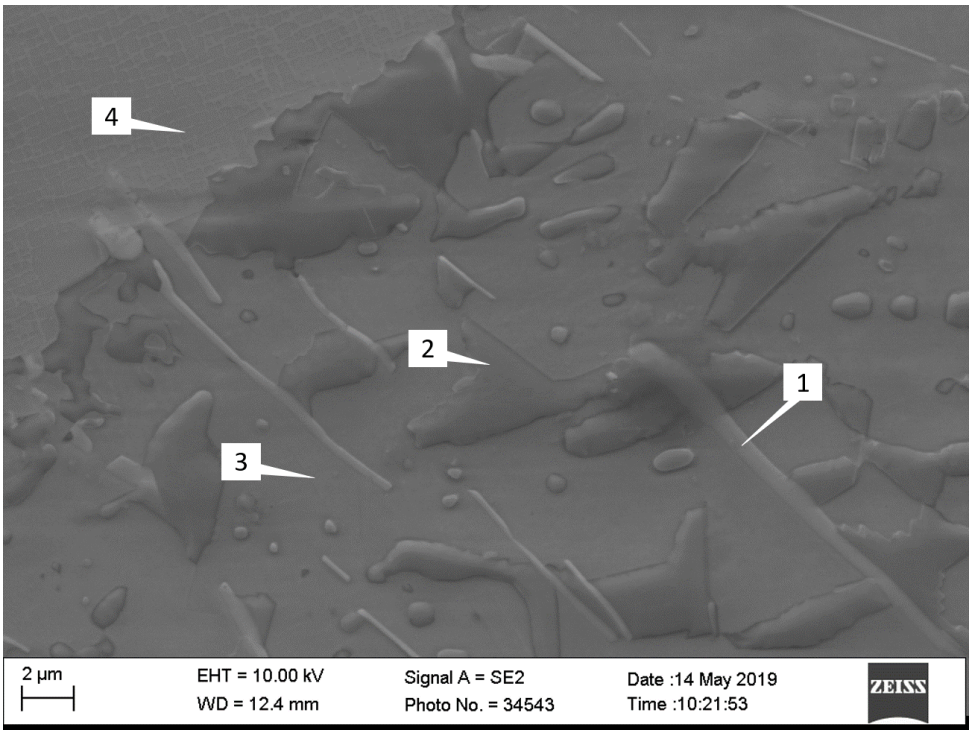

Figure 4.10: CMSX-4, 850°C, 500h. **1:** TaS_2, **2:** Cr-sulphide, **3:** Ni-rich matrix, **4:** Base material.

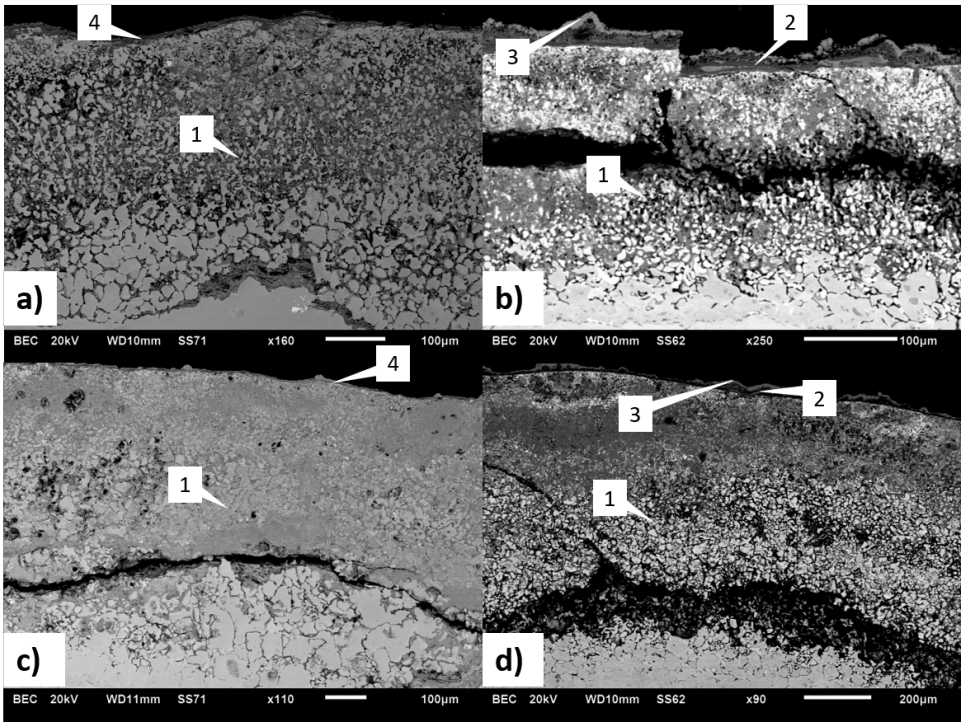

Figure 4.11: a) CM247, 850°C/300h. b) CMSX-4, 850°C/300h. c) CM247, 850°C/500h, d) CMSX-4, 850°C/500h. **1:** Cr-, Al-oxides, **2:** Al-oxide, **3:** NiO, **4:**Ni-, Al-oxide.

4.2.2 IN792

IN792 shows type I corrosion behaviour. After the first cycle there is a small amount of internal sulphidation and little to no internal oxidation. A thin porous non-protective oxide scale that also shows signs of spallation surrounds the material. This scale has a layered structure. The elements forming this oxide scale are mainly Al, Cr and Ti. Ni and Co are present in lower amounts in the outer surface.

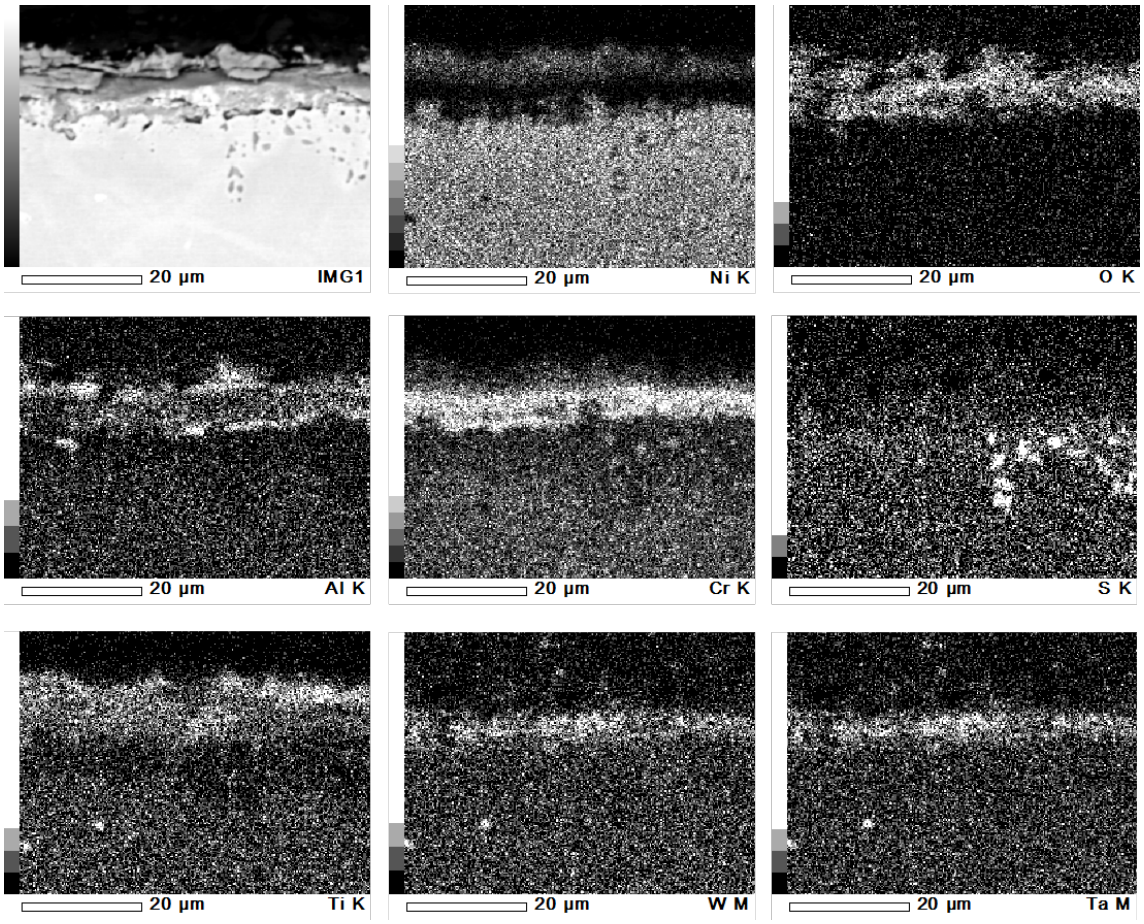

Figure 4.12: EDS elemental mapping of IN792, 850°C/100h

The corrosion attack increases severely after 300h. The sample shows, on its surface, areas of preferential oxidation at the bottom in the form of blisters. The blisters are round/oval shaped of various diameters up to 4 mm. The depth of penetration is considerably larger under the surface affected by the blisters. The internal oxidation products consist of mainly Al-oxides and Cr-oxides. Cr-sulphides and Ta-sulphides were found underneath the internal oxidation layer. No significant amount of Ti was found in the internal oxidation products under the blister (figure 4.13). Cr-sulphides are embedded on a Ni-rich matrix as it can be seen from figure 4.15.

After 1000h, the blisters increase their size and merge with each other. The larger blisters are located on top of the sample.

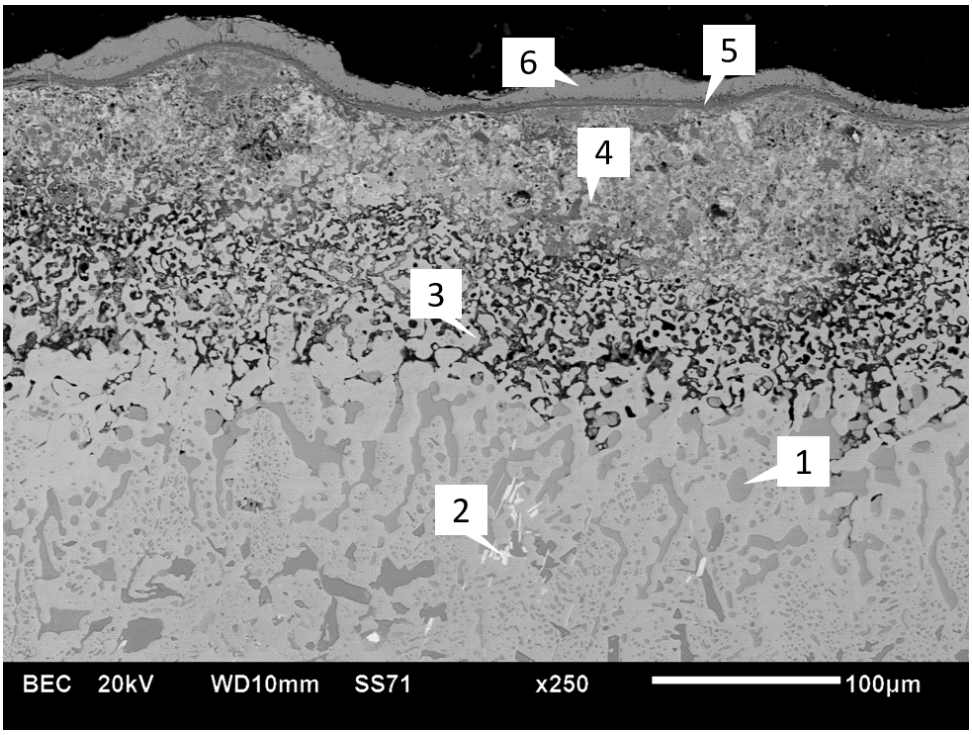

Figure 4.13: Blister corrosion products. IN792,850°C/300h. **1:** Cr-sulphide, **2:** TaS_2, **3:** Al-oxides, **4:** Cr-, Al-oxides, **5:** Al-oxide, **6:** Ni-oxide.

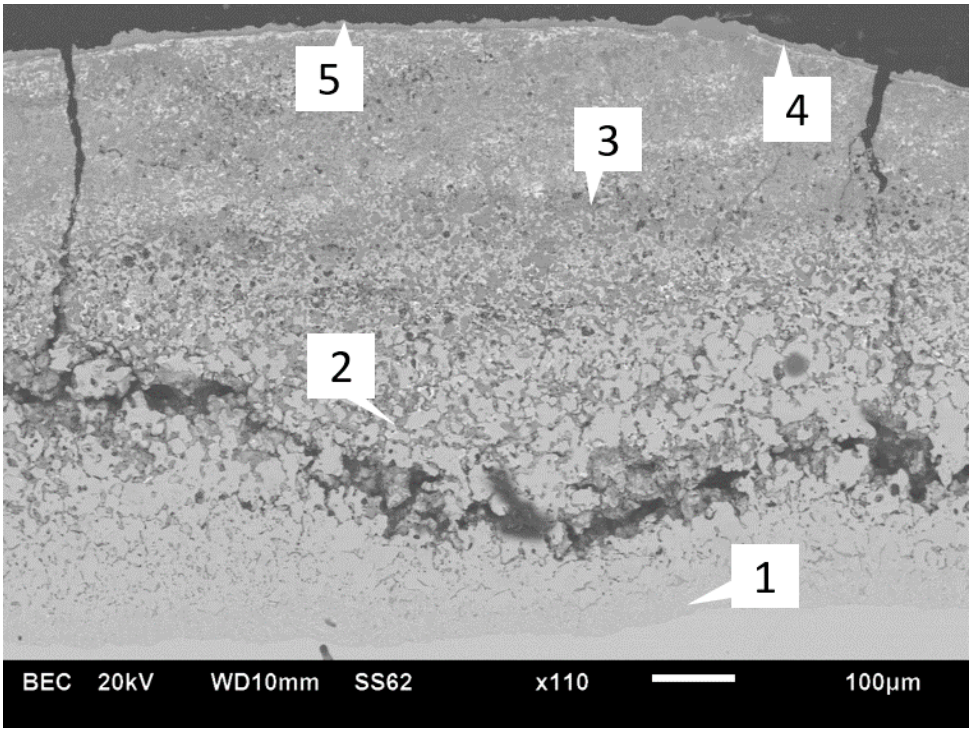

Figure 4.14: IN792, 850°C/1000h. **1:** Cr-sulphides, **2:** Al-oxide, **3:** Cr-, Al-oxide, **4:** Ni-W-oxide, **5:** NiO.

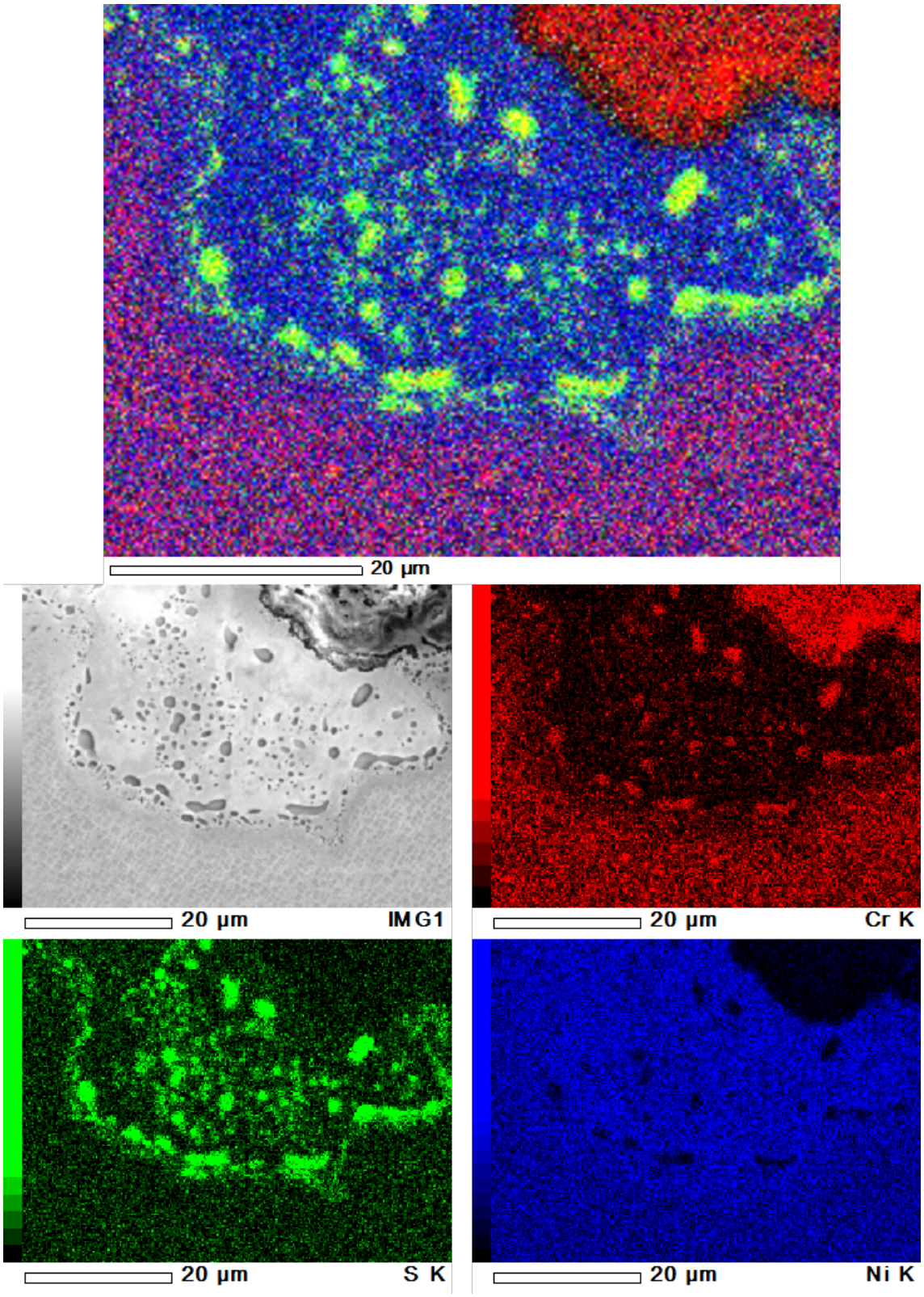

Figure 4.15: Elemental mapping overlay and individual maps of IN792, 850°C/500h

4.2.3 Alloys A-1 and A-2

Alloy A-1 does not show the same resistance to corrosion as IN792. After 100h, the material has already formed blisters on its bottom side causing a large loss of cross-sectional area.. Internal oxidation is mainly composed of Cr-oxides. Al-oxides are found in contact with the metal in areas where the blistering is non-existing. Alloy A-2 forms a more compact external oxide layer in comparison with A-1. It consists on Ni-, Cr- and Al-oxides. The layer is non-protective, nonetheless. A-2 shows no blistering which means the depth of the attack is not as large as in A-1. Carbides appear to be a site where preferential oxidation occurs (figure 4.16).

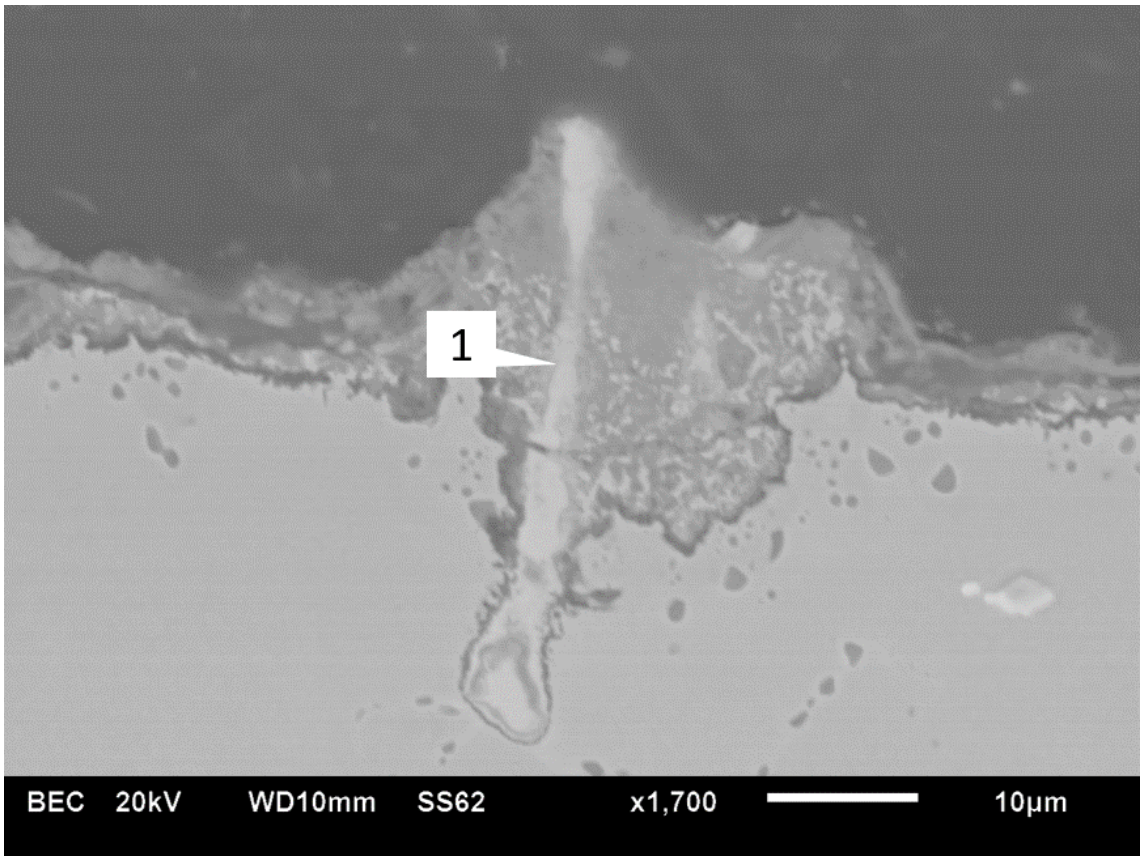

Figure 4.16: Alloy A-2, 850°C/100h. **1:** Trapped carbide.

After 300h, alloy A-2 shows no significant growth or change in the oxide scales, neither in the internal oxidation products. Meanwhile, A-1 shows detachment of the external oxide scale from the internal oxidation products.
At 500h, both materials show the same type I corrosion morphology and have developed blisters in the bottom side of the sample. Alloy A-2 had a significantly larger blister.

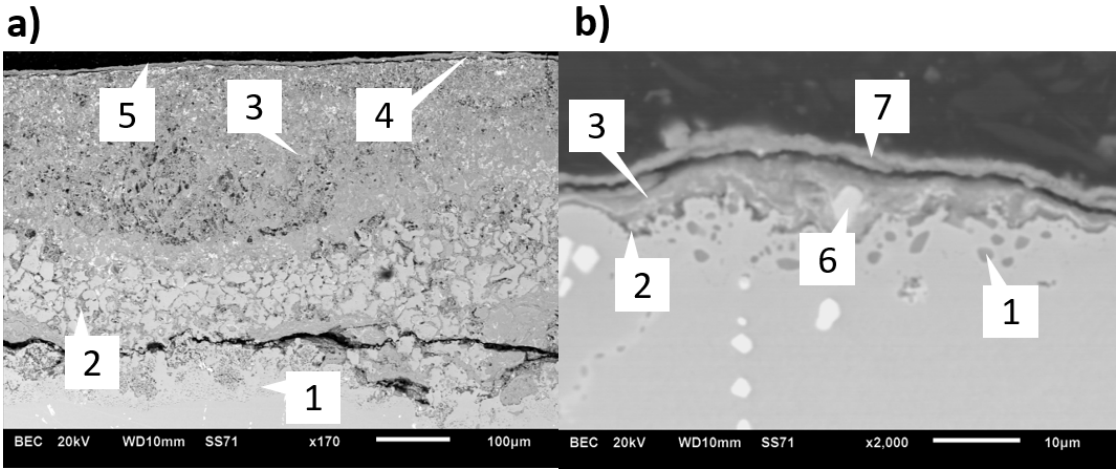

Figure 4.17: a) A-1 850°C/100h. b) A-2 850°C/100h. **1:** Cr-sulphide, **2:** Al-oxide, **3:** Cr-, Al-oxide, **4:** Ni-W-oxide, **5:** NiO, **6:** Carbide, **7:** Ni-, Cr-, Al-oxide.

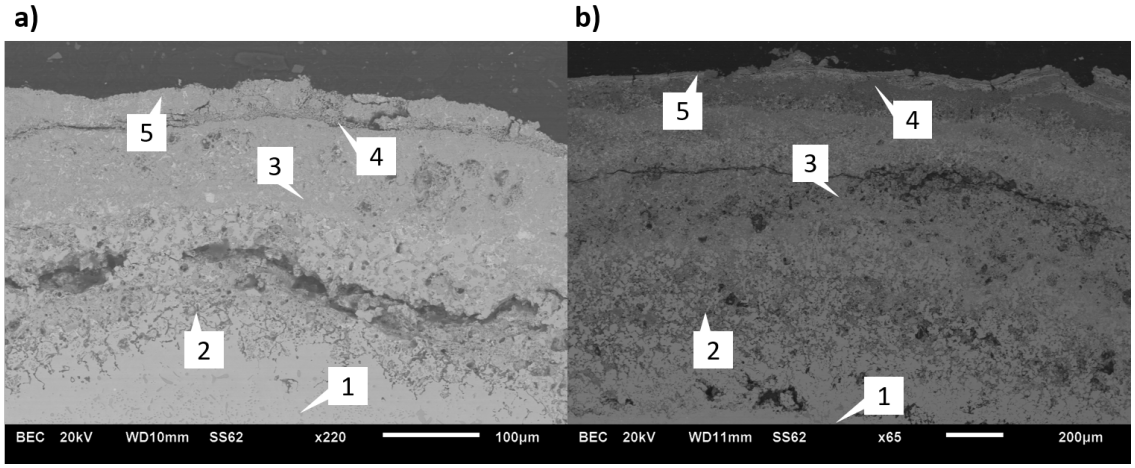

Figure 4.18: a) A-1 850°C/500h. b) A-2 850°C/500h. **1:** Cr-sulphide, **2:** Al-oxide, **3:** Cr-, Al-oxide, **4:** Al-oxide, **5:** Cr-, Al-oxide.

4.2.4 Alloy B

Alloy B is still in incubation stage after 100h. The sample formed a double scale that consists of Ni-, Cr- and Al-oxides. The outer oxide scale has a higher concentration of Ni than the inner one. The scales are not dense and show signs of spallation (figure 4.19).
After 300h, the material has reached propagation stage showing the characteristic morphology of type I hot corrosion. The outer oxide scale is composed of NiO and it shows deficient adhesion at the metal-scale interface. Internal sulphidation is evident and there is no sign of Ta-sulphides in contrast with IN792 which formed TaS_2 after the same amount of cycles. The internal sulphidation products are composed mainly of Cr- and Al-oxides. At 500h, the material suffers from blistering. As mentioned

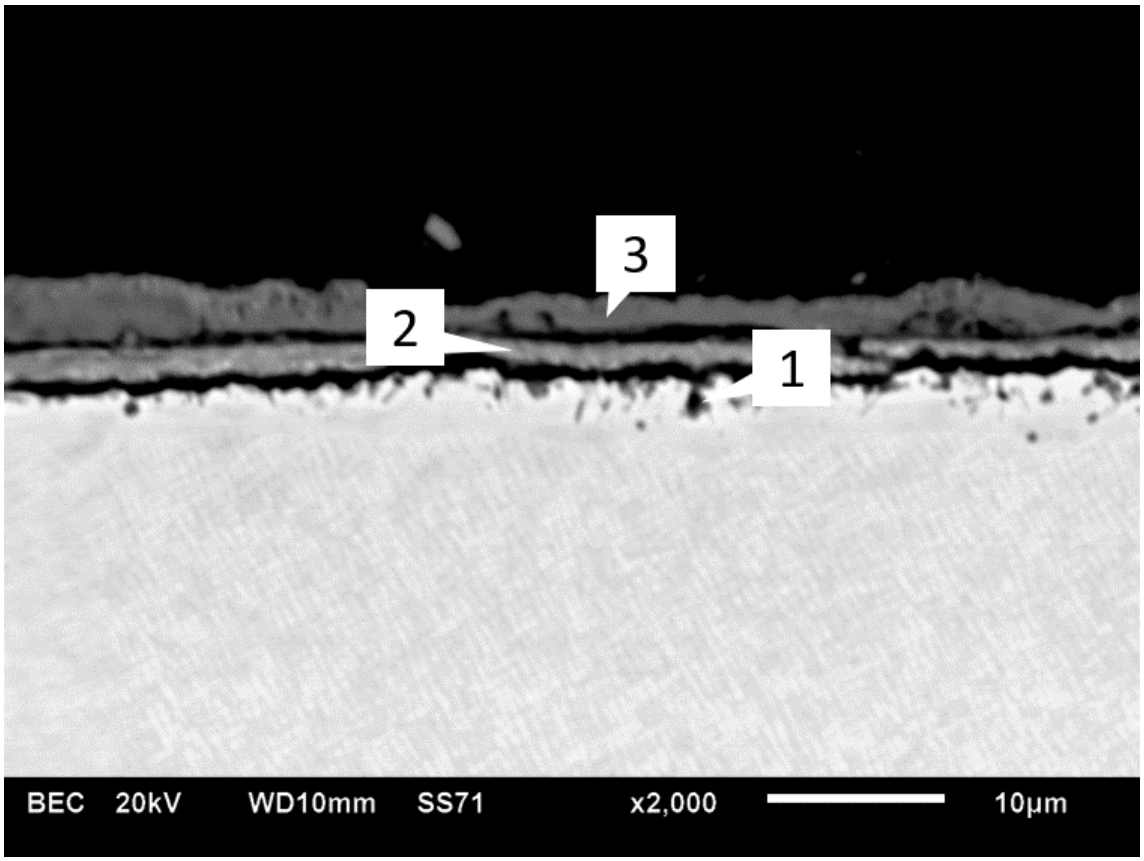

Figure 4.19: Alloy B, 850°C/100h. **1:** Al-oxide, **2:** Cr-, Al-oxide,**3:** Ni-, Cr-, Al-oxide

before, the cross-sectional area under the blister have a greater depth of penetration in comparison to the other surfaces. After 1000h, the loss of cross section due to blistering is catastrophic.

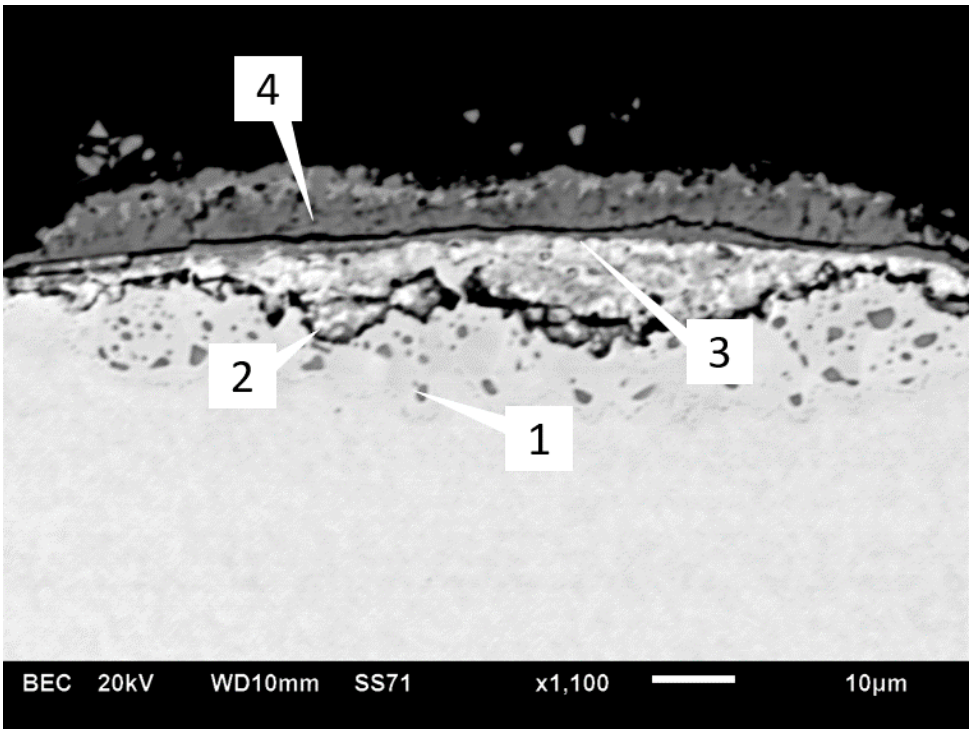

Figure 4.20: Alloy B, 850°C/300h. **1:**Cr-sulphides, **2:** Al-oxide, **3:** Ni-W-oxide, **4:** Cr-, Al-oxide.

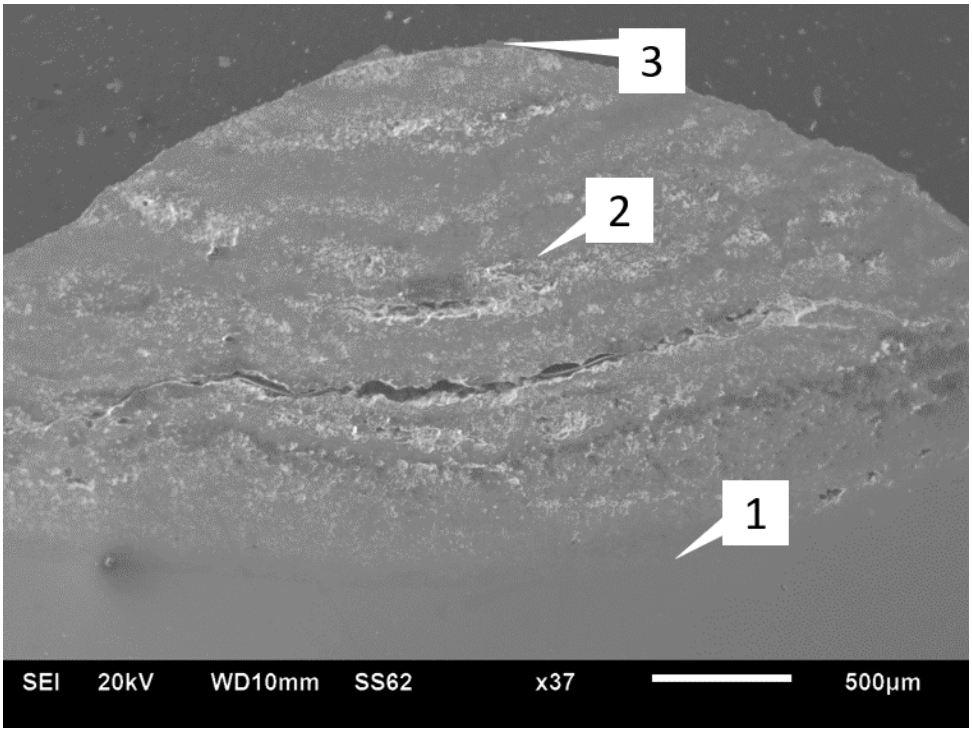

Figure 4.21: Alloy B, 850°C/1000h. **1:**Cr-sulphides, **2:**Cr-, Al-oxides, **3:**NiO.

5

Discussion

This chapter consists on two sections. In the first one, a general reaction mechanism is proposed for each temperature (700°and 850°C) to describe the hot corrosion process in all the alloys. In the second section, the alloys were organized into three groups (according to the similarities in their behaviour) to describes the particularities that govern their corrosion resistance.

5.1 General reaction mechanism

A reaction mechanism is proposed for all the alloys based on the experimental results and a literature study.

5.1.1 Corrosion test at 700°C

The incubation stage starts when the salt deposit comes in contact with the passive oxide scale formed by the metal. The oxide is NiO. Via acidic fluxing, the scale forms a low melting eutectic of composition Na_2SO_4−MSO_4, where M is Ni [40, 41]. The partial pressure of SO_3 is higher at lower temperatures at a constant gas composition. This allows the $NiSO_4$ component to be formed from the following reaction:

$$NiO + SO_3 \longrightarrow NiSO_4 \tag{5.1}$$

And in terms of the moving species, it becomes:

$$NiO + Na_2SO_4 \longrightarrow Ni^{2+} + {SO_4}^{2-} + Na_2O \tag{5.2}$$

The formation rate of $NiSO_4$ is related to the partial pressure of SO_3. It can also be deducted that the amount of $NiSO_4$ that is formed is directly proportional to the amount of Na_2SO_4. The melting temperature of the Na_2SO_4−$NiSO_4$ eutectic is 671°C [42] which means a molten solution is created. Refractory metal oxides (RMO) such as MoO_3 are formed simultaneously. These RMO react with the molten solution to form Na_2MoO_4.

$$Na_2SO_4 + MoO_3 \longrightarrow Na_2MoO_4 + SO_3 \tag{5.3}$$

The molten solution increases its acidity with the addition of MoO3.

The molten solution has become a corrosive melt due to its double acidic components: MoO_3 and SO_3. The corrosive melt is capable of dissolving cations in the

oxide and incorporating them into it. Ions such as Al_3^+, Cr_3^+ and Ni_2^+ are incorporated from their respective oxides. These ions will precipitate away from the high activity zone of MoO_3 which is at the gas interface [43]. This creates a porous non-protective external oxide scale. Which acidic component dominates the dissolution depends on which reaction yields the highest solubility. The amount of oxide dissolved is determined by the values of the activity of the MoO_3 (a_{MoO_3}) and the partial pressure of SO_3 (p_{SO_3}). MoO_3 evaporates at the gas interface. The reaction is considered to be self-sustaining due to the fact that the corrosive melt has a supply of MoO_3 directly from the material, hence it does not need an external source of MoO_3.

As the external oxide scale thickens, a_{MoO_3} decreases which fulfils the Rapp-Goto criterion[1]. This deceleration of the reaction will convert the corrosive melt to a solid compound made of $NiMoO_4$ [45].

$$NiO + Na_2MoO_4 \longrightarrow NiMoO_4 + Na_2O \tag{5.4}$$

$$Na_2O + Ta_2O_5 \longrightarrow 2\,NaTaO_3 \tag{5.5}$$

[45] proposes the formation $NaTaO_3$ as a retainer of Na_2O which inhibits the formation of Na_2MoO_4. In this study the formation of this compound is inconclusive.

5.1.2 Corrosion test at 850°C

A reaction mechanism for type I hot corrosion for Ni-base superalloys that fits the results of this study was proposed by [30].

The incubation stage starts with the salt deposit reacting with the passive oxide layer that is formed beneath it (Cr_2O_3). Through basic fluxing, the scale and the deposit form Na_2CrO_4.

$$Na_2SO_4 + Cr_2O_3 \longrightarrow Na_2CrO_4 + CrS + \frac{3}{2}\,O_2 \tag{5.6}$$

The O_2 is used to form NiO.

At 850°C, the partial pressure of SO_2 is high enough for it to penetrate into the metal matrix through the oxide scale and form sulphides. The two mechanisms by which this can occur are called *chemical diffusion* and *physical permeation*. Sulphide formation from chemical diffusion occurs when the chemical potential of SO_2 in the gas phase is higher than the chemical potential needed to form the sulphide in the metal at the metal-scale interface. For physical permeation to result in internal sulphidation, it is necessary that the partial pressure of SO_2 is high enough to trigger the reaction with the metal at the metal-scale interface [46].

The formation of a protective scale depends on the concentration of the alloying element that can form this passive layer. If the concentration is too low, then

[1]The Rapp-Goto criterion stablishes that for the continued hot corrosion of a pure metal the gradient of solubility of the protective oxide in the salt film is negative at the oxide-salt interface. This is what allows the oxide to precipitate as discontinuous particles [44].

internal oxidation will occur instead of an external oxide layer. This leaves the surface of the alloy susceptible to react with the atmosphere. This can result in the formation of base-metal oxides or a duplex scale of base-metal oxides and sulphides. Sulphur is now available to diffuse through the internal oxidation zone and start sulphidizing the alloying elements. When the concentration of the alloying element that forms a passive oxide scale is sufficient, the reaction rates are slow until the scale is penetrated by sulphur. When sulphur permeates the passive oxide layer, it may find itself in a zone with low oxygen potential at the metal-scale interface. If the oxygen potential is low enough, this may lead to the formation of base-metal sulphides or alloying element sulfides [47]. In [48], it was found that SO_2 can penetrate Cr_2O_3 physically through cracks and pores.

Similar to type II, the corrosive melt reacts with RMO and, thus, increases the acidity of the melt. In addition, this leads to the the formation of porous external Cr-oxide scales.

$$Na_2CrO_4 + WO_3 \longrightarrow Na_2WO_4 + Cr_2O_3\,(\text{porous}) \tag{5.7}$$

From this moment, the reaction shifts from basic fluxing to self-sustained acidic fluxing. As the internal oxidation of the metal proceeds, the Cr-sulphides are oxidized creating Cr_2O_3 and the sulphur is free to react with more chromium. As it was seen in CMSX-4 and IN792, it is also possible to form TaS_2. According to [49], TaS_2 formation requires a lower partial pressure of oxygen than CrS and Ta and Cr both show a high affinity for sulphur. The reaction reaches a deceleration period as shown in eq. 5.4.

5.2 Alloy-specific behaviour

5.2.1 CM247 and CMSX-4

Alloys CM247 and CMSX-4 are alumina-forming alloys which are designed to have excellent creep resistance while sacrificing corrosion resistance which is done mostly by reducing the amount of Cr. At 700°C, they present type II hot corrosion morphology while at 850°C, they exhibit type I hot corrosion morphology. In general, both alloys perform poorly in terms of corrosion resistance. However, CMSX-4 has a slower corrosion rate and is less affected than CM247. This can be due to two things: CMSX-4 single crystal structure reduced the rate of corrosion by not allowing the diffusion of reactant along the grain boundaries which requires a lower activation energy than the diffusion through the lattice; and CMSX-4 has no carbides in its microstructure. The oxidation of carbides has been proven to be an initiation site for hot corrosion [30, 50]. Carbides with refractory metals such as W and Mo form oxides when they come in contact with the melt and form WO_3 and MoO_3 which increase the acidity of the melt and promote acidic fluxing. In addition, [30] proposes that carbides affect the formation of a protective oxide scale by causing Cr depletion around them leading to a Cr deficit at the moment of forming the scale. The products of the oxide scale are composed mainly by NiO and Cr-, Al-oxides for tests at 700°C and Ni-W-oxides and Ni-, Cr-, Al- oxides at 850°C. Ta can act

as "sulphur catcher" and according to [49] has a similar affinity to sulphur as Cr. However, Ta is a heavy element and it is not desirable to increase the density of the material.

5.2.2 IN792, Alloy A-1 and A-2

IN792 is material well known for its high temperature capabilities including its mechanical properties and high temperature oxidation and corrosion resistance. The latter is attributed to its high Cr content which allows it to form a protective Cr_2O_3 scale. Alloys A-1 and A-2 have also a high Cr content in addition to high Al. Even though the amount of Cr is larger than the Al, Cr facilitates alumina forming so Al_2O_3 is formed as the protective oxide scale instead of Cr_2O_3. In order to prevent extra mass gain from oxidation at high temperatures, Ti is not present in Alloy A-1. Alloy A-1 had the worst corrosion resistance out of these three alloys. The absence of Ti and the formation of an Al_2O_3 are good design philosophies for oxidation resistance but they are not so good in terms of corrosion resistance. [51] reported that, in fact, Ti has a positive effect on the hot corrosion resistance. This may be an indication of why IN792 and Alloy A-2 performed better. Alloy A-1 may have a better performance at higher temperatures where the oxidation rate is higher (figure 2.3) and it can form SiO_2 which is thermodynamically stable and can form a protective oxide scale above 1000°C.

5.2.3 Alloy B

Alloy B has a single crystal structure. It follows the same design philosophy as Alloy A-1 by increasing its Cr content to increase corrosion resistance and removing Ti to reduce the mass gain due to high temperature oxidation. It also forms preferentially a protective Al_2O_3 scale. It forms similar products as IN792: an external Cr-, Al-oxide scale with NiO at the scale-gas interface, but presents a slower corrosion rate, mainly due to its lack of grain boundaries, possibly to its larger Cr content and lower refractory metal content (Mo and W) which increase the acidity of the corrosive melt leading to self-sustained acidic fluxing. As for to other carbide forming alloys corrosion may be promoted by oxidation of carbides.

6
Conclusions

In the present work, we evaluated progression of hot corrosion in different materials used in industrial gas turbines. The investigated alloys were CM247, CMSX-4, IN792 and three alloys developed by Siemens.

Hot corrosion testing was performed using furnace testing. The atmosphere to which the samples were exposed consisted of a gas mixture of 300 ppm vol. SO_2-14,8% O_2-N_2. The samples were sprayed with a eutectic mixture of Na_2SO_4/K_2SO_4. This led to a more aggressive corrosion attack. All alloys were tested at 700 and 850°C.

Corrosion mechanism was proposed for each temperature based on the obtained results and a literature study.

At 700°C all alloys underwent type II hot corrosion. Type II corrosion is dependent on the partial pressure of SO_3 which dictates the corrosion rate and the type of corrosion products formed. The partial pressure of SO_3 is higher at lower temperatures. The activity of SO_3 is promoted by the presence of of Na_2SO_4 and a sulphur-containing atmosphere. comes from the salt deposit. The corrosion mechanism of type II hot corrosion is based on acidic fluxing. The process starts with the salt deposit dissolving the initial oxide scale and creating a molten solution with refractory metal oxides (i.e. MoO_3,WO_3) which incorporate other metallic ions into the solution. The outer oxide scales are formed by these ions precipitating far from the acid activity of the melt which is high at the metal-melt interface and low near the gas phase.

At 850°C, all alloys underwent type I hot corrosion. At this temperature, the partial pressure of SO_2 is high enough for it to physically penetrate the passive oxide scale through pores and cracks. This allows for the formation of sulphides in the metal. Carbides were identified as a cause of disturbing the formation of a continuous passive oxide scale. This mechanism was enhanced by the eutectic deposit mixture. The salt deposit melted and created a molten solution with the passive oxide scale. The scale dissolves through basic fluxing [30]. Then it follows a similar path as the type II corrosion as refractory metals generate the acidic flux. As the internal sulphides are oxidized, sulphur is free to diffuse through the metal in search of alloying elements with which to react (i.e. Cr or Ta).

Alloy CM247 was found to be the worst performing material in terms of corrosion resistance. This is due to its creep-resistance oriented design. CMSX-4 shows a better performance at early cycles but at later stages, it performs similar to CM247.

This better performance at the early stages may be due to its lack of carbides and grain boundaries. Alloy "A-2" performs better than Alloy "A-1" but not as good as IN792. The reason behind this behaviour may be linked to the chemical composition with the major difference being that "Alloy A-2" contains Ti. Alloy "B" performs similarly as IN792.

Future work can be focused on identifying the phases of the oxides that were found in both the inner oxidation layer and the outer scales. This can be done by using X-ray diffraction (XRD) and Transmission Electron Microscopy (TEM). Weight gain/loss measurements would provide additional information especially for cases in which spallation and/or blistering is severe.

Bibliography

[1] M. P. Boyce. "Advanced industrial gas turbines for power generation". In: *Combined Cycle Systems for Near-Zero Emission Power Generation*. Elsevier Masson SAS., 2012, pp. 44–102. ISBN: 9780857090133. DOI: 10.1016/B978-0-85709-013-3.50002-X. URL: http://dx.doi.org/10.1533/9780857096180.44.

[2] Wikipedia. *Brayton's cycle*. 2019. URL: https://en.wikipedia.org/wiki/Brayton_cycle.

[3] Siemens AG. *Meeting your needs , driving your profitability : Industrial gas turbines from Siemens*. Erlangen, 2009.

[4] "Superalloys for gas turbine engines". In: *Introduction to aerospace materials*. Ed. by Adrian P Mouritz. Woodhead Publishing, 2012, pp. 251–267. ISBN: 9781855739468. DOI: https://doi.org/10.1533/9780857095152.251.(http://www.sciencedirect.com/science/article/pii/B9781855739468500121).

[5] Jonas Saarimäki. "Effect of Dwell-times on Crack Propagation in Superalloys". PhD thesis. Linköping University, 2015. ISBN: 9789176858714. DOI: 10.3384/lic.diva-123306.

[6] Nader El-bagoury. "Ni based superalloy: casting technology, metallurgy, development, properties and applications". In: April (2016).

[7] H. K. D. H. Bhadeshia. *Nickel Based Superalloys*. 2019. URL: https://www.phase-trans.msm.cam.ac.uk/2003/Superalloys/superalloys.html.

[8] Jonas Saarimäki. *Cracks in superalloys*. 1897. 2018, pp. 1–108. ISBN: 9789176853856. DOI: https://doi.org/10.3384/diss.diva-144397.

[9] Juraj Belan. "GCP and TCP Phases Presented in Nickel-base Superalloys". In: *Materials Today: Proceedings* 3.4 (2016), pp. 936–941. ISSN: 22147853. DOI: 10.1016/j.matpr.2016.03.024. URL: http://dx.doi.org/10.1016/j.matpr.2016.03.024.

[10] A.K. Jena and M.C. Chaturvedi. "Role of Alloying Elements for Nickel Superalloys". In: *Journal of Materials Science* 19 (1984), pp. 3121–3139. ISSN: 00222461. DOI: 10.1007/BF00549796.

[11] M. Hansen and K. Anderko. *Constitution of binary alloys*. 2nd. McGraw-Hill, 1958.

[12] Roman Sowa, Sebastian Arabasz, and Magdalena Parlinska-Wojtan. "Classification and microstructural stability of high generation single crystal Nickel-based superalloys". In: *Zastita materijala* 57.2 (2016), pp. 274–281. ISSN: 0351-9465. DOI: 10.5937/zasmat1602274s.

[13] P. N. Quested and S. Osgerby. "Mechanical properties of conventionally cast, directionally solidified, and single-crystal superalloys". In: *Materials Science*

and Technology 2.5 (2014), pp. 461–475. ISSN: 0267-0836. DOI: 10.1179/mst.1986.2.5.461.

[14] G.H. Meier. "High Temperature Oxidation and Corrosion of Metal-Silicides". PhD thesis. 1986, p. 17. DOI: 10.1557/proc-81-443.

[15] B.S. Mitchell. *An introduction to materials engineering and science for chemical and materials engineers*. John Wiley, 2004.

[16] University of Cambridge. *The Ellingham diagram*. 2018. URL: https://www.doitpoms.ac.uk/tlplib/ellingham_diagrams/ellingham.php.

[17] Haiping Lai. "High Temperature Oxidation and Corrosion of Ni-Based Superalloys for Industrial Gas Turbines". PhD thesis. 2014.

[18] Neil Birks, Gerald Meier, and Frederick Pettit. "Mechanisms of oxidation". In: *High-Temperature Oxidation of Metals*. 2006, p. 40.

[19] William Smith and Javad Hashemi. "Solidification and crystalline imperfections". In: *Foundations of materials science and engineering*. 2011, pp. 156–159.

[20] Per Kofstad. *High temperature corrosion*. Elsevier Science Publishing, 1988.

[21] Neil Birks, Gerald Meier, and Frederick Pettit. "Mechanisms of oxidation". In: *High-Temperature Oxidation of Metals*. 2006, p. 64.

[22] Pavleta Knutsson, Haiping Lai, and Krystyna Stiller. "A method for investigation of hot corrosion by gaseous Na2SO4". In: *Corrosion Science* 73 (2013), pp. 230–236. ISSN: 0010938X. DOI: 10.1016/j.corsci.2013.04.006. URL: http://dx.doi.org/10.1016/j.corsci.2013.04.006.

[23] L. G. Johansson. *High Temperature Corrosion Course*. 2014.

[24] Samuel Cruchley, Hugh Evans, and Mary Taylor. "An overview of the oxidation of Ni-based superalloys for turbine disc applications: surface condition, applied load and mechanical performance". In: *Materials at High Temperatures* 33.4-5 (2016), pp. 465–475. ISSN: 09603409. DOI: 10.1080/09603409.2016.1171952.

[25] J. H. Chen, P. M. Rogers, and J. A. Little. "Oxidation behavior of several chromia-forming commercial nickel-base superalloys". In: *Oxidation of Metals* 47.5-6 (1997), pp. 381–410. ISSN: 0030770X. DOI: 10.1007/BF02134783.

[26] Neil Birks, Gerald Meier, and Frederick Pettit. "Oxidation of alloys". In: *High-Temperature Oxidation of Metals*. 2006, pp. 116–118.

[27] Neil Birks, Gerald Meier, and Frederick Pettit. "Oxidation of alloys". In: *High-Temperature Oxidation of Metals*. 2006, p. 122.

[28] P.Y. Hou. "Oxidation of Metals". In: *Shreir's Corrosion*. Ed. by J.A.R. Tony. Elsevier: Oxford, 2010, pp. 195–239.

[29] Neil Birks, Gerald Meier, and Frederick Pettit. "Oxidation of alloys". In: *High-Temperature Oxidation of Metals*. 2006, p. 124.

[30] B Bordenet. "High Temperature Corrosion in Gas Turbines: Thermodynamic Modelling and Experimental Results". PhD thesis. 2004. URL: %5C%5CKwi-server%5Cliteratur%5Cedo%5Carticles%5CDSH%5CDSH_0866.pdf.

[31] George Y. Lai. "Sulfidation". In: *High Temperature Corrosion and Material Applications*. 2007, pp. 201–234. DOI: 10.1361/hcma2007p201.

[32] G Lai. "Hot Corrosion in Gas Turbines". In: *ASM International: High Temperature Corrosion and Materials Application*. 2007, pp. 249–258. DOI: 10.1361/hcma2007p249. URL: www.elsevier.com/locate/engfailanal%0Ahttp:

//www.asminternational.org/documents/10192/3459328/5208_Chap_09.pdf/ebd7d964-5c1c-4f9a-ae65-21c70214ea7c.

[33] Neil Birks, Gerald Meier, and Frederick Pettit. "Hot corrosion". In: *High-Temperature Oxidation of Metals*. 2006, p. 205.

[34] Neil Birks, Gerald Meier, and Frederick Pettit. "Hot Corrosion". In: *High-Temperature Oxidation of Metals*. 2006, p. 207.

[35] Frederick Pettit and Gerald Meier. "Oxidation and hot corrosion of superalloys". In: *Superalloys 1984*. Ed. by M. Gell. 1984, pp. 651–687.

[36] Celal Cingi and Jouko J Vuorinen. *CM 247 LC superalloy microstructure and heat treatment*. Tech. rep. 1993.

[37] K. Harris, G.L. Erickson, and R.E. Schwer. *MAR M 247 Derivations - CM 247 LC DS Alloy and CMSX Single Crystal Alloys: Properties & Performance*. Tech. rep. 1984, pp. 221–230. DOI: 10.7449/1984/superalloys{_}1984{_}221{_}230.

[38] K. Harris et al. "Development of two rhenium- containing superalloys for single- crystal blade and directionally solidified vane applications in advanced turbine engines". In: *Journal of Materials Engineering and Performance* 2.4 (1993), pp. 481–487. ISSN: 10599495. DOI: 10.1007/BF02661730.

[39] Beining Du et al. "Investigation on the microstructure and tensile behavior of a Ni-based IN792 superalloy". In: *Advances in Mechanical Engineering* 10.2 (2018), pp. 1–8. ISSN: 16878140. DOI: 10.1177/1687814017752167.

[40] Pongpat Lortrakul et al. "Investigation of the mechanisms of Type-II hot corrosion of superalloy CMSX-4". In: *Corrosion Science* 80 (2014), pp. 408–415. ISSN: 0010938X. DOI: 10.1016/j.corsci.2013.11.048. URL: http://dx.doi.org/10.1016/j.corsci.2013.11.048.

[41] A. Encinas-Oropesa. "A Study of hot corrosion of single crystal superalloys and platinum-aluminide coatings." PhD thesis. 2005, p. 250.

[42] Karl Petter Lillerud and Per Kofstad. "Sulfate-induced hot corrosion of nickel". In: *Oxidation of Metals* 21.5-6 (1984), pp. 233–270. ISSN: 0030770X. DOI: 10.1007/BF00656835.

[43] Neil Birks, Gerald Meier, and Frederick Pettit. "Hot Corrosion". In: *High-Temperature Oxidation of Metals*. 2006, pp. 226–228.

[44] Neil Birks, Gerald Meier, and Frederick Pettit. "Hot corrosion". In: *High-Temperature Oxidation of Metals*. 2006, p. 214.

[45] George C. Fryburg. "Chemical Reactions Involved in the Initiation of Hot Corrosion of B-1900 and NASA-TRW VIA". In: *Journal of The Electrochemical Society* 129.3 (2006), p. 571. ISSN: 00134651. DOI: 10.1149/1.2123928.

[46] Neil Birks, Gerald Meier, and Frederick Pettit. "Reactions of metals in mixed environments: Conditions for sulphide formation". In: *High-Temperature Oxidation of Metals*. 2006, pp. 188–196.

[47] Neil Birks, Gerald Meier, and Frederick Pettit. "Reactions of metals in mixed environments: Conditions for sulphide formation." In: *High-Temperature Oxidation of Metals*. 2006, p. 198.

[48] R. E. Lobnig et al. "Sulfur in chromia". In: *Oxidation of Metals* 39.5-6 (1993), pp. 353–370. ISSN: 0030770X. DOI: 10.1007/BF00664661.

[49] J. X. Chang et al. “Role of tantalum in the hot corrosion of a Ni-base single crystal superalloy”. In: *Corrosion Science* 98 (2015), pp. 585–591. ISSN: 0010938X. DOI: 10.1016/j.corsci.2015.05.066. URL: http://dx.doi.org/10.1016/j.corsci.2015.05.066.

[50] I. Gurrapa et al. “The Importance of Hot Corrosion and Its Effective Prevention for Enhanced Efficiency of Gas Turbines”. In: *Gas Turbines - Materials, Modeling and Performance*. 2016, pp. 59–60.

[51] N. Eliaz, G. Shemesh, and R. M. Latanision. “Hot corrosion in gas turbine components”. In: *Engineering Failure Analysis* 9.1 (2002), pp. 31–43. ISSN: 13506307. DOI: 10.1016/S1350-6307(00)00035-2.

A

Appendix

A.1 Alloys that presented visible internal oxidation

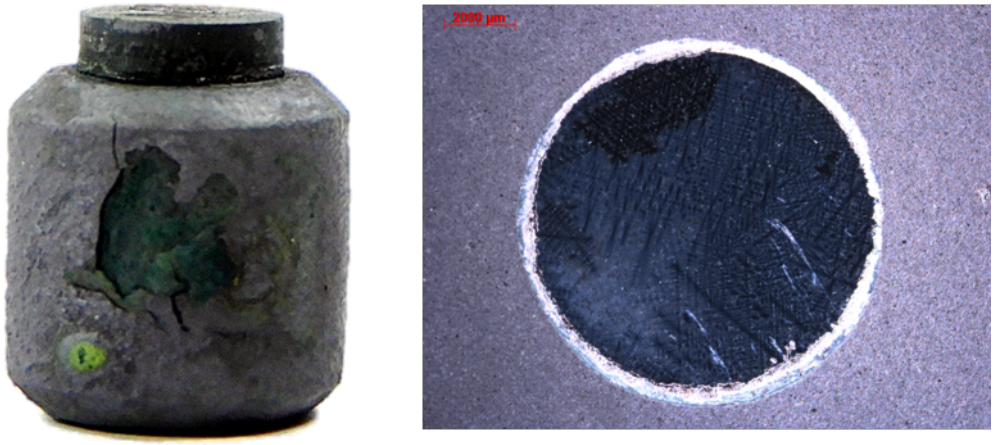

Figure A.1: Photos of the exposed samples and cross-section view of CM247, 850°C/300h

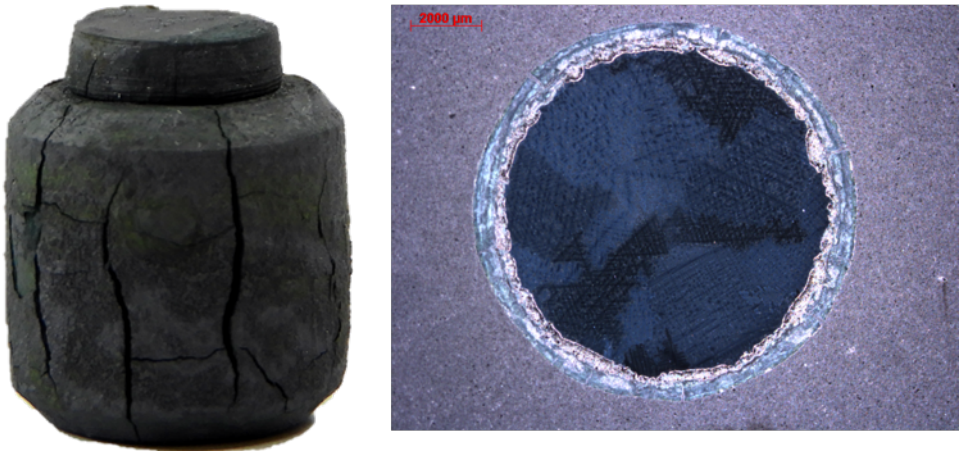

Figure A.2: Photos of the exposed samples and cross-section view of CM247, 850°C/500h

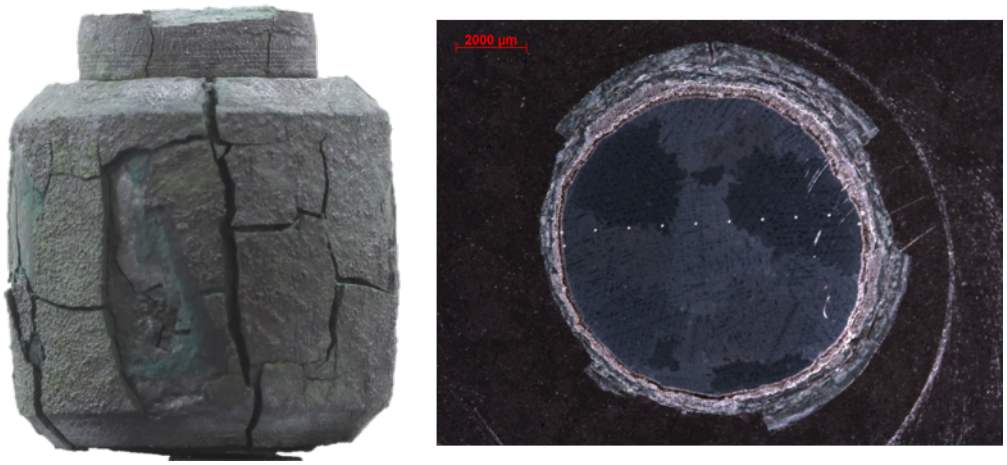

Figure A.3: Photos of the exposed samples and cross-section view of CM247, 850°C/1000h

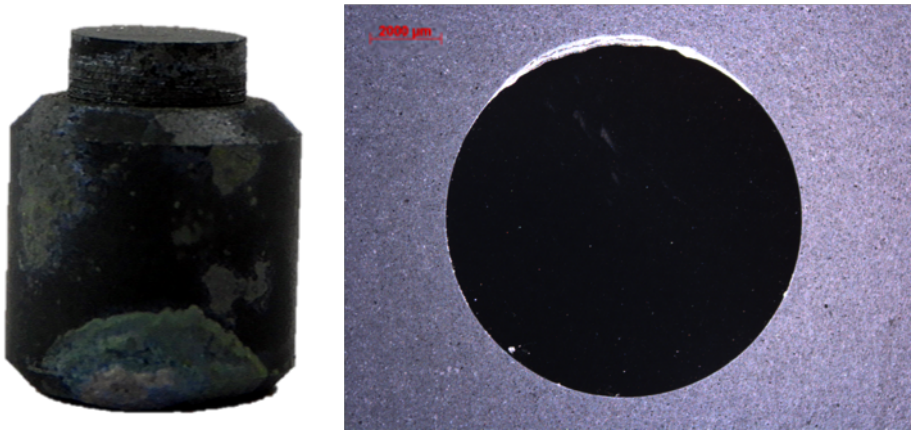

Figure A.4: Photos of the exposed samples and cross-section view of CMSX-4, 850°C/300h

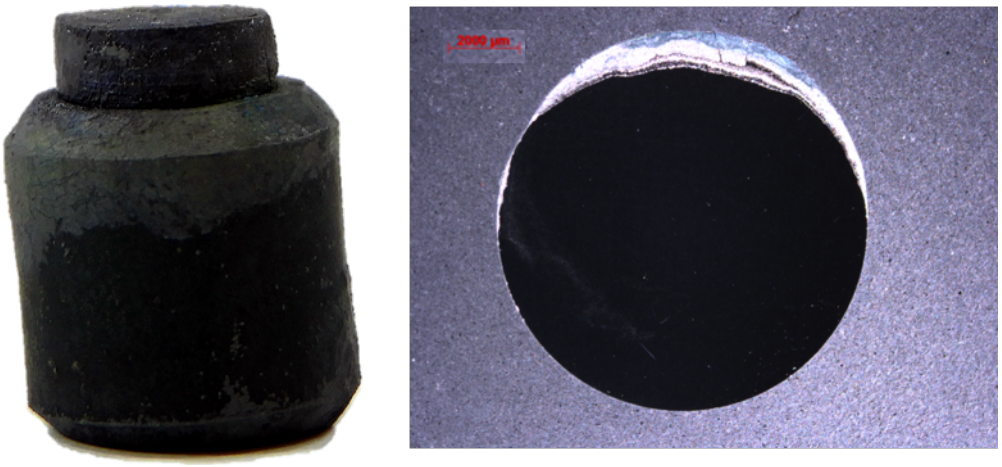

Figure A.5: Photos of the exposed samples and cross-section view of CMSX-4, 850°C/500h

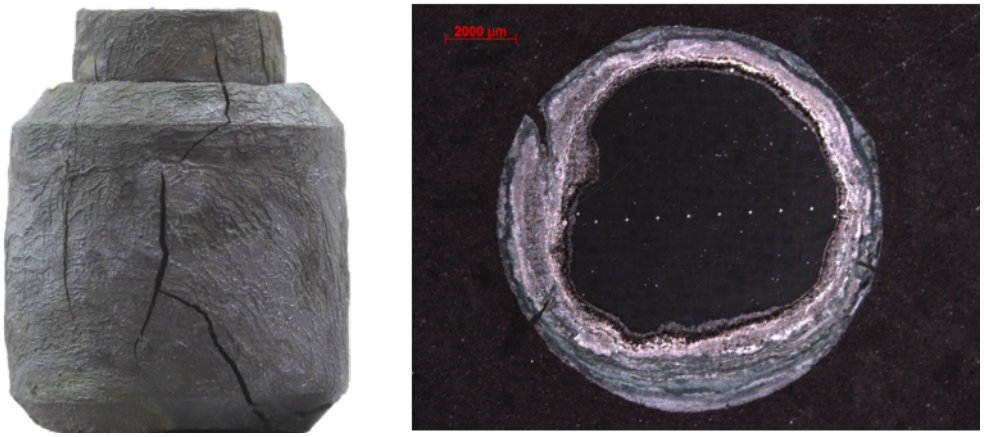

Figure A.6: Photos of the exposed samples and cross-section view of CMSX-4, 850°C/1000h

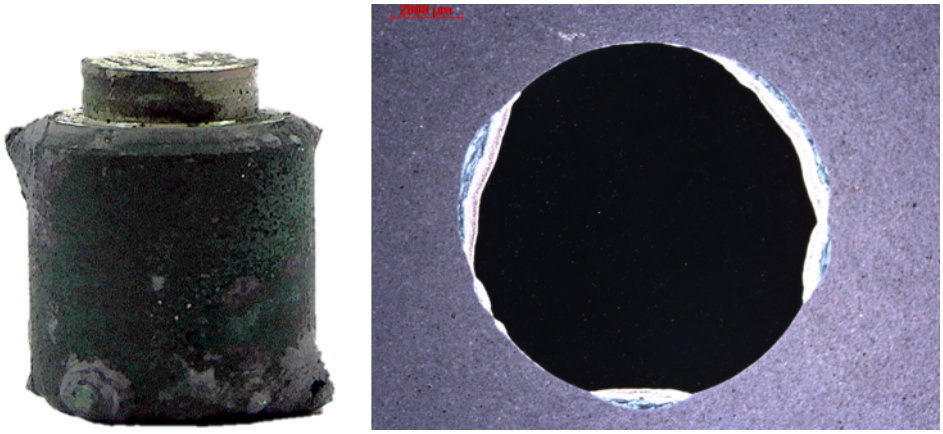

Figure A.7: Photos of the exposed samples and cross-section view of Inconel 792, 850°C/300h

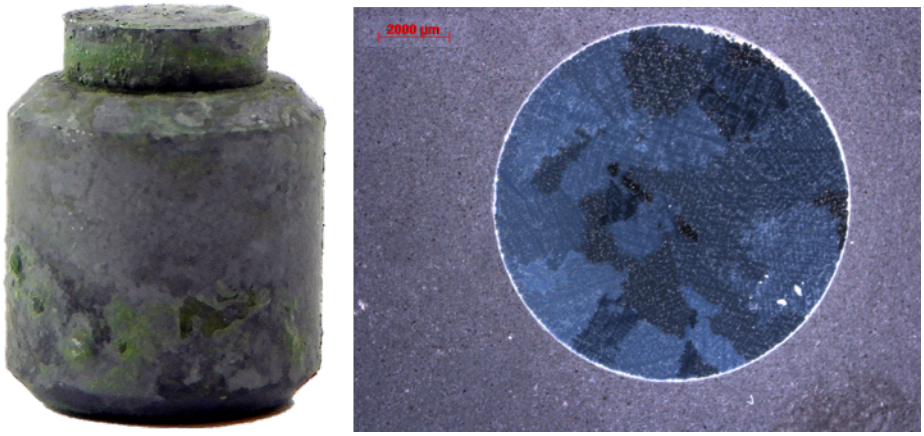

Figure A.8: Photos of the exposed samples and cross-section view of Inconel 792, 850°C/500h

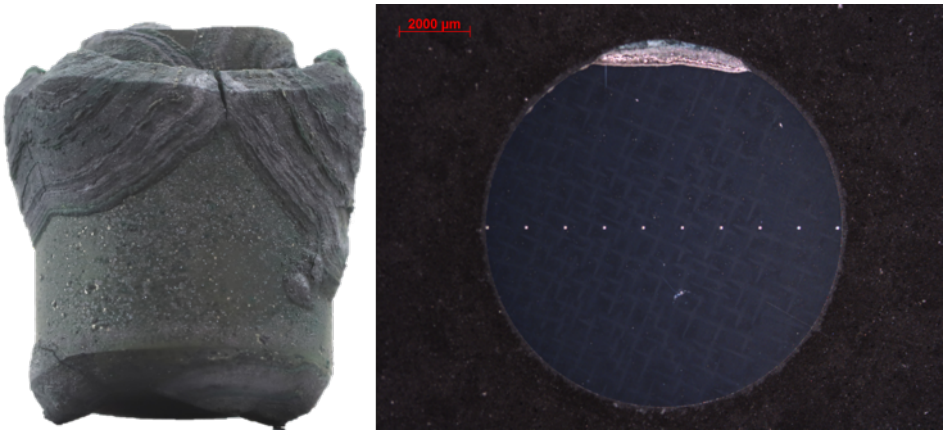

Figure A.9: Photos of the exposed samples and cross-section view of Inconel 792, 850°C/1000h

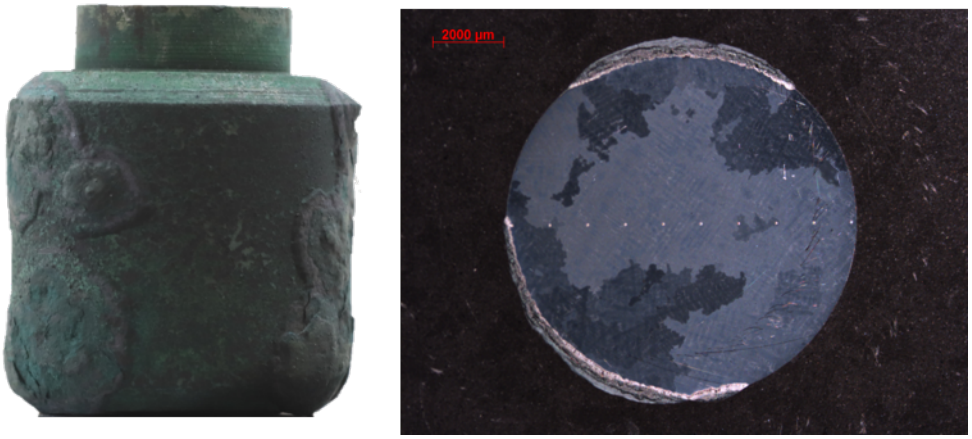

Figure A.10: Photos of the exposed samples and cross-section view of alloy A-1, 850°C/100h

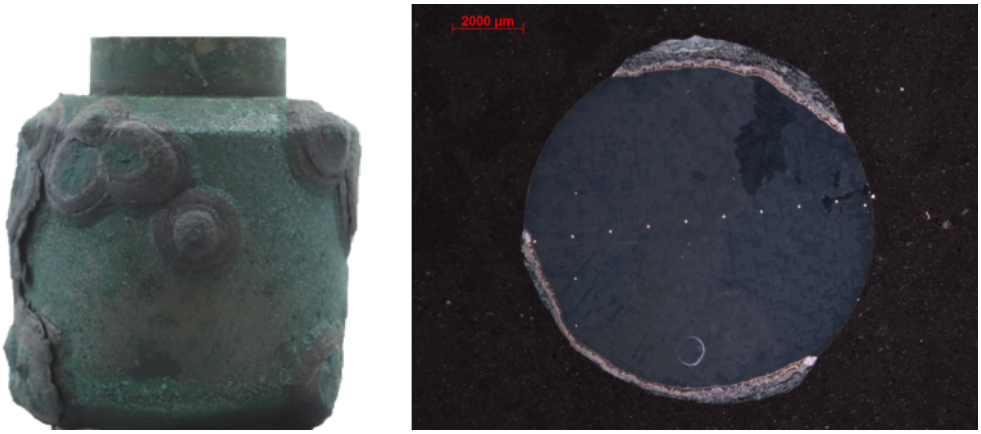

Figure A.11: Photos of the exposed samples and cross-section view of alloy A-1, 850°C/300h

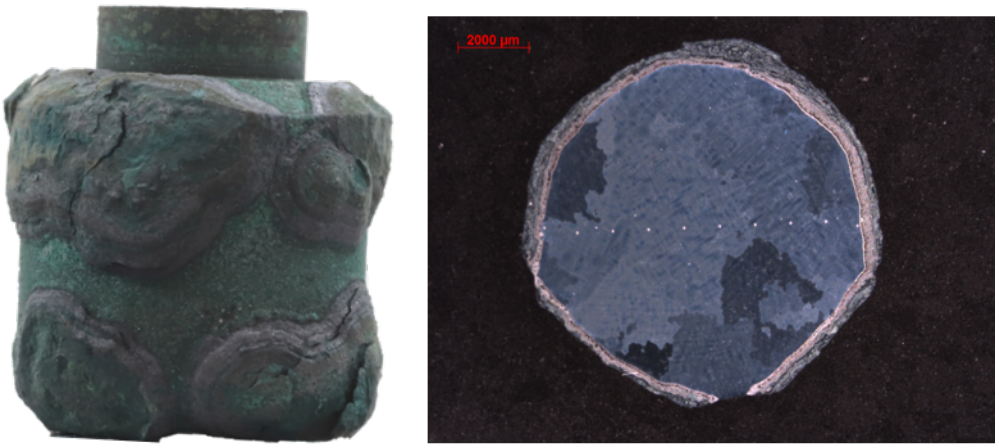

Figure A.12: Photos of the exposed samples and cross-section view of alloy A-1, 850°C/500h

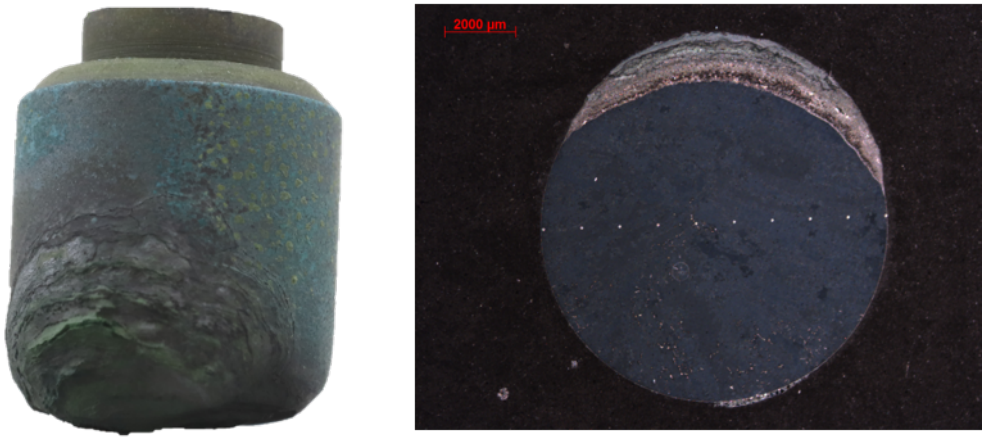

Figure A.13: Photos of the exposed samples and cross-section view of alloy A-2, 850°C/500h

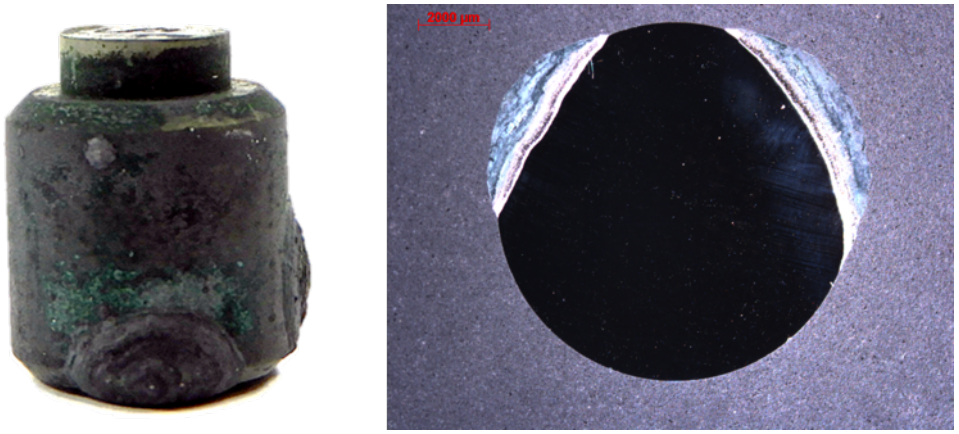

Figure A.14: Photos of the exposed samples and cross-section view of alloy B, 850°C/500h

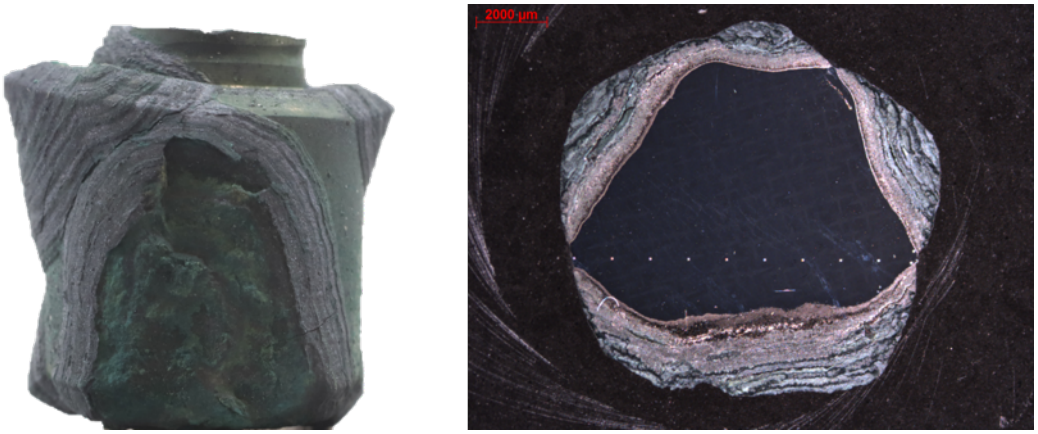

Figure A.15: Photos of the exposed samples and cross-section view of alloy B, 850°C/1000h